nature physics

Article

https://doi.org/10.1038/s41567-024-02460-w

Polarity-driven three-dimensional spontaneous rotation of a cell doublet

Received: 21 December 2022

Accepted: 29 February 2024

Published online: 13 May 2024

Check for updates

Linjie Lu[1,2,3,4,11], Tristan Guyomar[1,2,3,4,11], Quentin Vagne[5,11], Rémi Berthoz[1,2,3,4], Alejandro Torres-Sánchez[6], Michèle Lieb[1,2,3,4], Cecilie Martin-Lemaitre[7,8], Kobus van Unen[9], Alf Honigmann[7,8,10], Olivier Pertz[9], Daniel Riveline[1,2,3,4] ✉ & Guillaume Salbreux[5] ✉

Mechanical interactions between cells play a fundamental role in the self-organization of organisms. How these interactions drive coordinated cell movement in three dimensions remains unclear. Here we report that cell doublets embedded in a three-dimensional extracellular matrix undergo spontaneous rotations. We investigate the rotation mechanism and find that it is driven by a polarized distribution of myosin within cell cortices. The mismatched orientation of this polarized distribution breaks the doublet mirror symmetry. In addition, cells adhere at their interface through adherens junctions and with the extracellular matrix through focal contacts near myosin clusters. We use a physical theory describing the doublet as two interacting active surfaces to show that rotation is driven by myosin-generated gradients of active tension whose profiles are dictated by interacting cell polarity axes. We also show that three-dimensional shape symmetries are related to broken symmetries of the myosin distribution in cortices. To test for the rotation mechanism, we suppress myosin clusters using laser ablation and generate new myosin clusters by optogenetics. Our work clarifies how polarity-oriented active mechanical forces drive collective cell motion in three dimensions.

Spontaneous cell rotational motions have been reported in a variety of contexts in vivo. For instance, tissues undergo rotation during development in *Drosophila* in the egg chamber[1], in the ommatidia of the retina[2], in the genitalia[3] and in zebrafish embryos, where rotation of cell pairs occurs in the zebrafish's lateral line[4]. In early *Caenorhabditis elegans* embryo development, chiral counter-rotating flows break chiral symmetry and play a role in setting the organism's left–right axis[5,6].

Seminal observations in vitro in two dimensions have shown that endothelial adhering cells migrating on a substrate and confined within a two-dimensional pattern form a stably rotating doublet[7]. The cell–cell interface adopts a curved shape, such that the doublet acquires an overall shape reminiscent of a 'yin–yang' symbol. More recently, groups of epithelial cells were reported to undergo rotation within rings[8,9]. In three dimensions in vitro, during alveologenesis of human mammary gland organoids, it has been shown that branches also undergo rotation[10]. In addition, Madin–Darby canine kidney (MDCK) cells can assemble into hollow cysts in three dimensions, which undergo spontaneous rotation in an assay within two layers of Matrigel[11]. There, the two layers of Matrigel impose a polarization axis to the cyst, which allows one to probe for chiral broken symmetry, revealed in a bias in the direction of

[1]Institut de Génétique et de Biologie Moléculaire et Cellulaire, Illkirch, France. [2]Université de Strasbourg, Illkirch, France. [3]Centre National de la Recherche Scientifique, Illkirch, France. [4]Institut National de la Santé et de la Recherche Médicale, Illkirch, France. [5]University of Geneva, Geneva, Switzerland. [6]Tissue Biology and Disease Modelling Unit, European Molecular Biology Laboratory, Barcelona, Spain. [7]Max Planck Institute of Molecular Cell Biology and Genetics, Dresden, Germany. [8]Technische Universität Dresden, Biotechnologisches Zentrum, Center for Molecular Cellular Bioengineering (CMCB), Dresden, Germany. [9]Institute of Cell Biology, University of Bern, Bern, Switzerland. [10]Cluster of Excellence Physics of Life, TU Dresden, Dresden, Germany. [11]These authors contributed equally: Linjie Lu, Tristan Guyomar, Quentin Vagne. ✉e-mail: riveline@unistra.fr; guillaume.salbreux@unige.ch

rotation. Altogether, rotational flow appears to be a common feature of the collective motion of interacting cells.

However, it is unclear how these rotational movements arise from the distribution of force-generating elements in the cell. Several models have been proposed to explain the rotation of a cell doublet on a two-dimensional substrate confined in a micropattern, using phase-field, particle-based or cellular Potts models[12–17]. These models exhibit simultaneous doublet rotation and/or interface deformation, based on a representation of actin polymerization forces and protrusion-forming forces[12–17], coupling to a biochemical system exhibiting spontaneous polarization through feedback between an activator and inhibitor[13] or to an internal polarization field[14,15]. Despite these advances, it is still unclear what biophysical mechanisms underlie collective cell rotation in three dimensions and, notably, how force-generating elements in the cell self-organize to drive coherent cell motion.

Dynamics of MDCK doublet rotation

In this Article, we describe the exploitation of a novel assay to study the mechanism behind the spontaneous rotation in three dimensions of MDCK cell doublets. We confined cells within a thin layer of Matrigel, close to the coverslip, to optimize imaging resolution (Fig. 1a and Methods). Strikingly, all embedded MDCK cell clusters undergo spontaneous rotation. We focus here on adhering cell doublets that emerge from the division of a single cell. There was no obvious common orientation of the axis of rotation of cell doublets, and in most but not all cases, a lumen at the cell–cell interface rotated with the doublet (Fig. 1b and Supplementary Videos 1 and 2). Single cells, instead, did not rotate in Matrigel (Extended Data Fig. 1). Cells participating in the rotating doublet, however, do not have to be sister cells, as two cells with different fluorescent E-cadherin labels could adhere to each other and initiate rotation (Fig. 1c and Supplementary Video 3). Doublet rotation was preserved following E-cadherin knockout (KO) (Extended Data Fig. 2 and Supplementary Video 4), suggesting also that E-cadherin-mediated adhesion was accompanied by other adherens junctions between cells presenting this doublet rotation[18].

To investigate quantitatively doublet rotation (Supplementary Sections 1 and 2), we imaged rotating doublets expressing E-cadherin and computationally segmented cell shapes in the doublet (Fig. 1d, Supplementary Video 5 and Methods). We calculated the centre of mass and velocity of each doublet cell, which allows the definition of a doublet rotation vector $\boldsymbol{\omega}$ (Fig. 1e). The norm of the rotation vector increased after cell division for ~100 min, before reaching a roughly constant rotational velocity of ~180° h^{-1} for a duration of ~10 h, corresponding to about five continuous full turns along the same direction (Fig. 1f,g). This is consistent with previously reported rotation velocities of MDCK cysts and breast epithelial cell spheres[11,19]. Plotting the trajectory of the vector $\boldsymbol{\omega}$ showed that the axis of rotation is not fixed but appears to drift over time (Fig. 1h and Extended Data Fig. 3). This is expected to the extent that no external cue sets a preferred axis of rotation. We note that this also implies that the spinning motion of the doublet does not intrinsically break chiral symmetry. Plotting the correlation function of the normalised rotation vector further indicated a characteristic correlation time of a few hours (Fig. 1i).

Dynamics of doublet elongation during rotation

We then wondered whether doublet cells were rotating relative to each other or were rotating together as a solid object (Fig. 2a). We reasoned that, in the latter case, the doublet elongation axis would rotate together with the rotation vector $\boldsymbol{\omega}$. We extracted from computationally segmented doublet shapes (Fig. 1d) the three orthogonal principal axes of elongation and evaluated the corresponding relative elongation magnitudes (Fig. 2b and Supplementary Section 3). We noted that the elongation of the doublet major axis was maximal at cell division and then relaxed to a nearly constant value, following the same trend as the magnitude of rotation, but in reverse (Figs. 1h and 2b). We then tested whether the rotation axis was correlated with the axis of maximal doublet elongation. This revealed a strong anti-correlation between the major axis of elongation and the direction of rotation (Fig. 2c), indicating that the elongation major axis is within the plane of rotation. The two minor cell elongation axes had, instead, weak positive correlations to the axis of rotation. The elongation major axis was also aligned with the vector joining the centre of mass of the cells, indicating that it rotates together with the doublet (Fig. 2c). Overall, these results suggest that the doublet rotates as a single physical object. Consistent with this idea, patterns of E-cadherin (Extended Data Fig. 4a,b, Supplementary Section 7 and Supplementary Video 5) and actin (Supplementary Video 6) at the cell–cell contact remained similar during ~1 h 30 min of observation.

Mode decomposition of interface deformation

We then quantified the shape of the interface between the two cells of the doublet (Fig. 2d). We found that the area of the interface reached a steady-state value and then remained constant for more than 7 h (Extended Data Fig. 4c). The average deviation of the interface from a planar shape was increasing with the magnitude of the doublet rotation (Fig. 2e,f). Cross-sections of the doublet showed that the interface was curved in a way that evoked a yin–yang shape, as noticed previously for doublets rotating on a substrate[7] (Fig. 1b–d). However, when looking at the full interface three-dimensional shape, we noticed that the shape was more complex than suggested by this simple picture (Fig. 2e). To make sense of this complex shape, we decomposed it into basic modes of deformations, which we obtained from Zernike polynomials and classified according to their symmetry properties (Fig. 2d and Supplementary Section 4). We defined a 'bowl' mode corresponding to a rotationally symmetric deviation of the interface, a 'saddle-node' mode with the symmetry properties of a nematic, a 'three-fold' mode with a three-fold rotation symmetry and a 'yin–yang' shape with a positive and a negative peak of deformation and the symmetry property of a vector (Extended Data Fig. 5a and Supplementary Section 4.2). We then measured the average magnitude of these four deformation modes (Fig. 2g). We found that all four modes contributed to the interface shape, while the saddle-node mode was dominant in relative magnitude (Fig. 2g). We then tested whether the orientations of the shape deformation modes were correlated with the axis of rotation (Fig. 2h). We calculated correlation values considering

Fig. 1 | Three-dimensional rotation of MDCK cell doublets. a, A schematic of the experimental assay. For each schematic cell doublet, blue ellipses correspond to nuclei, purple lines to cell–cell contacts and yellow lines to lumen. **b**, Snapshots of rotating doublets. Red arrows indicate the direction of rotation. E-cadherin-mNG is labelled in green and Podocalyxin-mScarlet in red. Time is relative to the beginning of Supplementary Video 1. **c**, Snapshots of a rotating doublet with two cells expressing E-cadherin of different colours. E-cadherin-GFP is shown in green and E-cadherin-DsRed in magenta. Time is relative to the beginning of Supplementary Video 3. **d**, Snapshots of a rotating doublet with labelled E-cadherin-mNG (green) (from top to bottom: cross-section, maximum projection and three-dimensional segmentation). $n = 14$ doublets and $N = 3$ biological repeats. Time is relative to cell division. **e**, Schematics for the calculation of the rotation vector $\boldsymbol{\omega}$ as a function of the centre of mass velocities $\mathbf{v}_1$, $\mathbf{v}_2$ and the vector $\mathbf{r}_{12}$ joining the cell centres (Supplementary Section 2). **f**, The magnitude ω of the rotational velocity as a function of time after cell division. **g**, Average and individual trajectories of the magnitude of the rotational velocity of cell doublets after cell division with $n = 14$ and $N = 3$. **h**, The trajectory of the rotation vector $\boldsymbol{\omega} = (\omega_x, \omega_y, \omega_z)$ normalised with respect to its maximum amplitude ω_{max}. The colour map indicates time, from dark blue to yellow. The grey sphere has unit radius. **i**, The autocorrelation of $\boldsymbol{\omega}_n = \boldsymbol{\omega}/\omega$ as a function of lag time with $n = 14$ and $N = 3$. Scale bars: 5 µm, except **b**: 20 µm. Time in panels **b**–**d** is in hh:mm. Error bars show the 95% confidence interval of the mean.

https://doi.org/10.1038/s41567-024-02460-w

the symmetry properties of each mode of deformation. Only the yin–yang mode, but neither the saddle-node nor three-fold mode, had an orientation correlated with the direction of rotation (Fig. 2h). Altogether, the doublet interface has a complex three-dimensional shape, and one mode of interface deformation correlated with the doublet rotation.

Cortical myosin distribution encoded in cell polarity

Having characterized the doublet rotation and the doublet interface shape, we then asked whether key proteins of the cytoskeleton and adhesion machinery had a distribution correlated with the doublet rotation. We stained cell doublets for phosphorylated myosin-regulatory

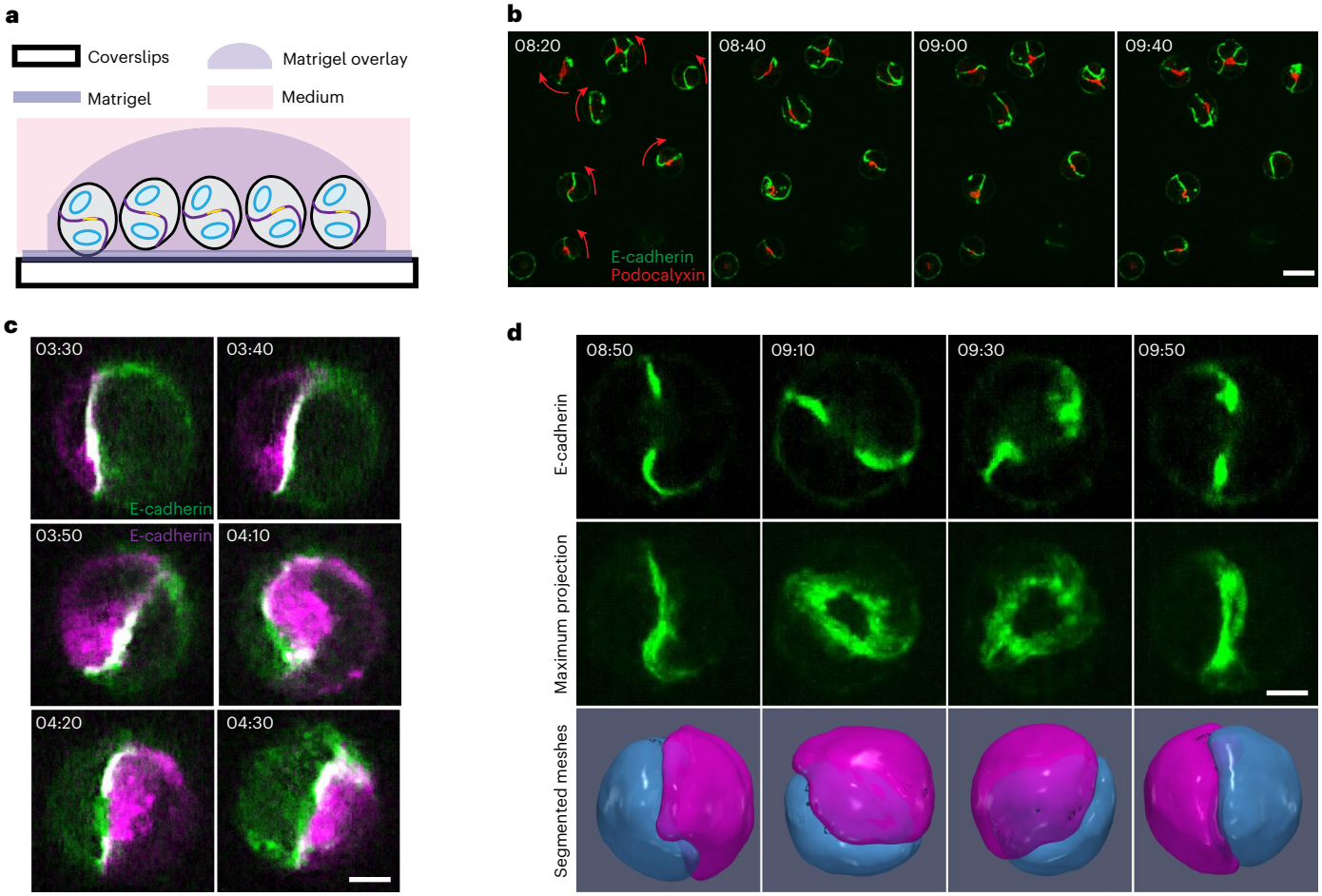

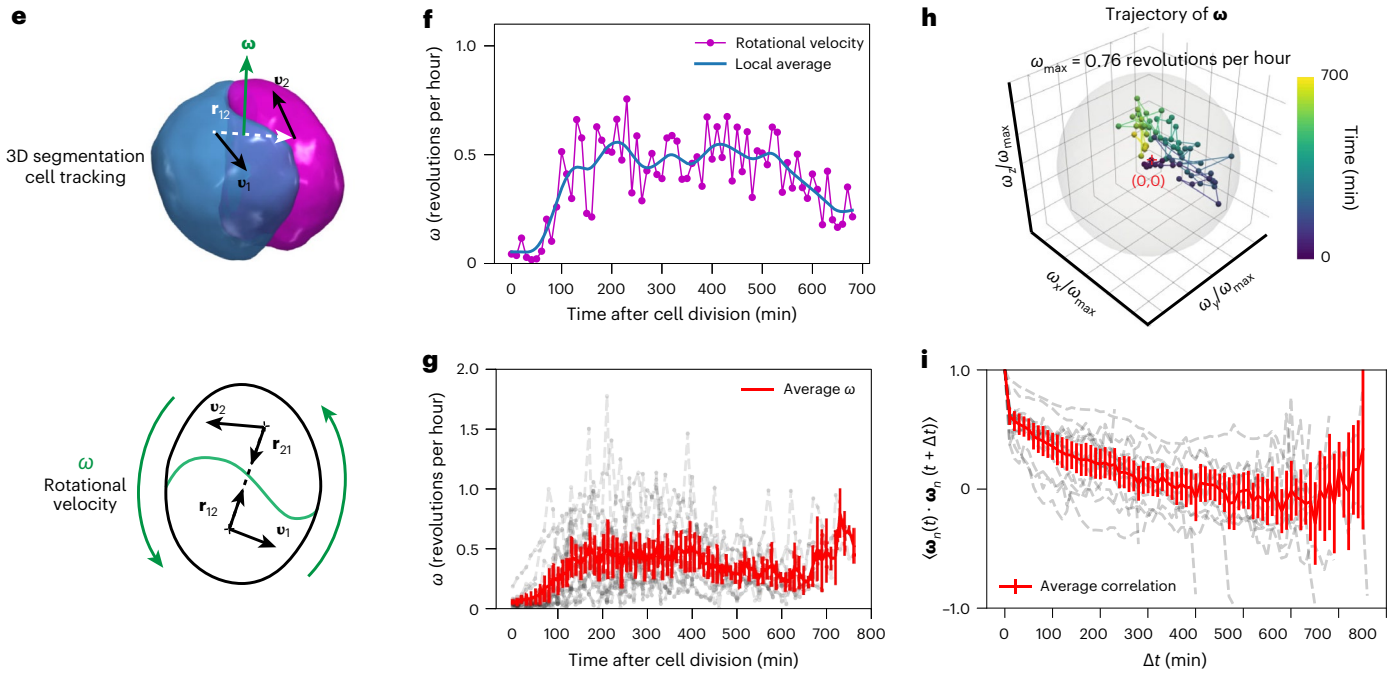

https://doi.org/10.1038/s41567-024-02460-w

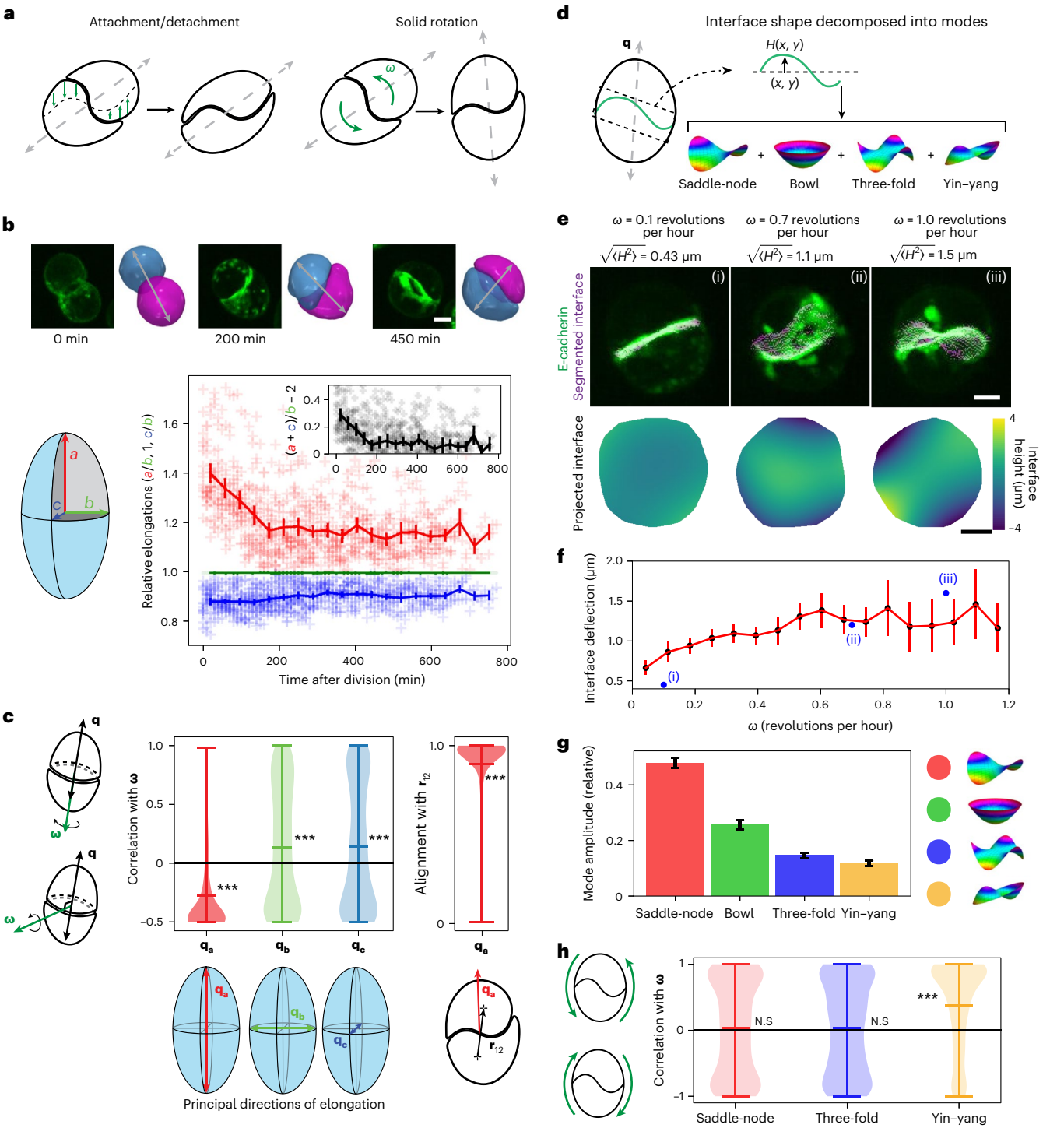

Fig. 2 | Coordinated rotation of doublet shape and interface. a, Schematics of possible scenarios of doublet rotation. Left: The interface is deforming (green arrows), leading to apparent rotation without motion of the doublet outer surface. Right: the doublet is rotating as a solid object and the doublet elongation axis (grey dotted line) rotates with the doublet. **b**, Top: snapshots of rotating doublets with labelled E-cadherin-mNG (green) and corresponding segmented meshes. Grey double arrows indicate the approximate elongation axis. Bottom left: a schematic for the definition of three doublet elongation axes *a*, *b* and *c*. Bottom right: relative doublet elongation magnitudes as a function of time after division (dots, individual data points; lines, connected binned averages). Inset: the ratio of elongation magnitudes, where positive values indicate a prolate shape. **c**, Left: the correlation of the axis of rotation with the axes of elongation $\mathbf{q} = \mathbf{q}_a, \mathbf{q}_b, \mathbf{q}_c$, as indicated in the schematics and defined in Supplementary Section 3. The direction of maximal elongation, $\mathbf{q}_a$, lies in the plane of rotation of the doublet. Right: the alignment of the elongation major axis $\mathbf{q}_a$ with the doublet axis $\mathbf{r}_{12}$. **d**, Schematics for decomposition of interface shape, quantified by height profile $H(x, y)$, into modes with different symmetries (colour code indicates height profile for visualization). **e**, Representative interface shape examples for different rotation magnitudes, corresponding to points indicated in **f**. Top: snapshots of E-cadherin-labelled doublets with overlaid interface segmentation, with the magnitude of the rotational velocity and average interface deflection presented above. Bottom: interface height map. **f**, The average interface deflection as a function of the magnitude of the rotational velocity. **g**, The average relative magnitude of the interface deformation modes. **h**, The correlation of the orientation of the deformation mode with the direction of rotation (indicated on the left by green arrows). Statistical tests (sign of the mean): $^{***}P < 10^{-4}$. Error bars show the 95% confidence interval of the mean with $n = 14$ doublets, $N = 3$ biological repeats and 780 data points in total.

https://doi.org/10.1038/s41567-024-02460-w

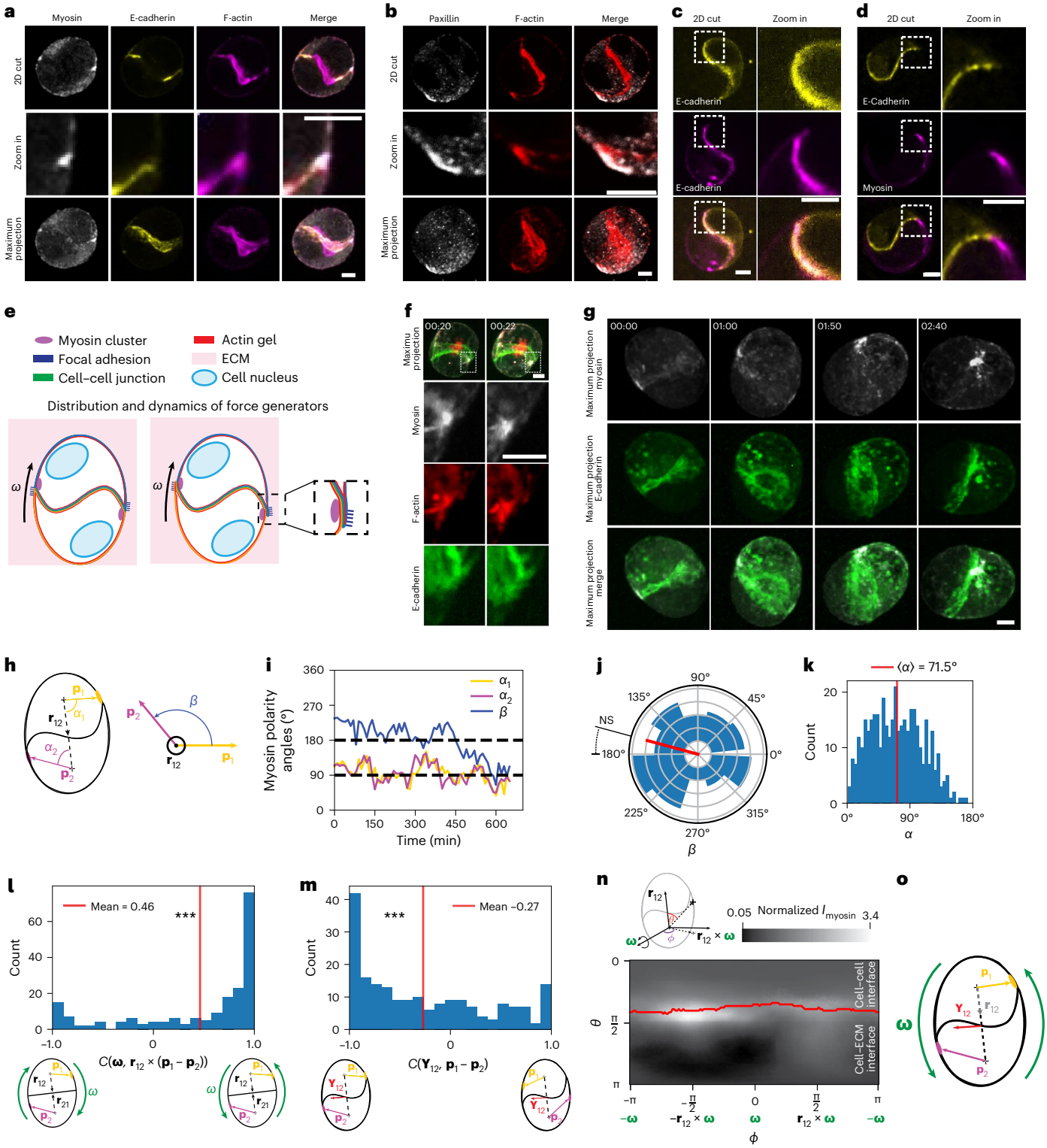

light chain (p-MRLC) to label active myosin, F-actin to label the actin cytoskeleton, E-cadherin to label cell–cell contacts and paxillin for focal contacts (Fig. 3a–d, Extended Data Fig. 6 and Methods). Strikingly, we found that, while E-cadherin and F-actin were largely concentrated at the cell–cell interface, p-MRLC was almost absent at the interface but concentrated at two bright zones near the boundary of the cell–cell junction. Immuno-fluorescence paxillin staining and live imaging of vasodilator-stimulated phosphoprotein (VASP) further revealed that focal contacts were also concentrated near the interface boundary (Fig. 3b and Extended Data Fig. 6c (VASP)). Live imaging combining markers for actin and myosin cytoskeleton, cell–cell adhesion and focal contacts showed that cadherins are recruited by both cells at the cell–cell interface, while myosin clusters and focal contacts appear distributed within the cortex on opposite sides near the doublet interface, judging from their position relative to the interface shape (Fig. 3a–g, Extended Data Fig. 4d, Supplementary Videos 6–10 and schematic in Fig. 3e). In some cases, myosin clusters appear to pull to deform locally the cell–cell interface (Fig. 3f, Extended Data Fig. 6a and Supplementary Video 10). Finally, the observed myosin dynamics (Extended Data Fig. 4d–h, Supplementary Section 8 and Supplementary Video 8)

https://doi.org/10.1038/s41567-024-02460-w

Fig. 3 | Distribution and dynamics of the force generators and adhesions in a cell doublet. a,**b**, Snapshots of representative examples of distribution of myosin, E-cadherin, F-actin and merge (**a**) and paxillin, F-actin and merge (**b**) with $n > 10$ doublets for **a** and **b**. **c**,**d**, Snapshots of a rotating doublet with two cells expressing proteins with different colours: E-cadherin-GFP (yellow) and E-cadherin-DsRed (magenta) showing that cadherin is recruited by interacting cells (**c**) and E-cadherin-DsRed (yellow) and MRLC-GFP (magenta) showing the relative localization of myosin and E-cadherin (**d**). Representative example of $n > 3$ doublets. **e**, Schematics of typical distributions of force-generating and adhesion proteins in the rotating doublet, also shown in a zoom. Orange and purple outlines represent individual cell outlines, small blue lines indicate focal adhesions. ECM, extracellular matrix. **f**, Snapshots of a rotating doublet labelled with myosin-KO1 (grey), SiR-Actin (red) and E-cadherin-mNG (green). Representative example of $n > 3$ doublets. The zoomed square region shows a myosin cluster apparently pulling the cell–cell interface (Supplementary Video 10). **g**, Snapshots of a rotating doublet labelled with E-cadherin-mNG (green) and myosin-KO1 (grey). **h**, The scheme of the myosin polarity angles α_1, α_2 and β. **i**, The myosin polarity angles with respect to the doublet axis as a function of time for a single doublet (dotted lines indicate 90° and 180°). **j**, A histogram of β, the angle between the polarity vectors of cells 1 and 2 projected on the plane orthogonal to $\mathbf{r}_{12}$. The red line indicates the average orientation of the distribution. NS, not significant. **k**, The histogram of α, the polarity angle relative to the doublet axis. **l**, A histogram for the correlation between the rotation vector $\boldsymbol{\omega}$ and the cross-product between the doublet axis and the difference of cell polarities. The red line shows the average. **m**, A histogram for the correlation between the yin–yang orientation vector and polarity difference. The red line shows the average. For **l** and **m**, see equations (43) and (44) in Supplementary Section 5.5 for a definition of the function C. **n**, A map of the average normalized myosin intensity (I_{myosin}) in spherical coordinates, in a reference frame defined by the rotation vector $\boldsymbol{\omega}$, the axis of the doublet $\mathbf{r}_{12}$ and their cross-product (θ and φ are spherical coordinates angles defined on schematics). The red line shows the averaged outer line of the cell–cell interface. **o**, A summary of the orientation of the myosin polarities and yin–yang interface deformation mode. Scale bars: 5 µm. Time in hh:mm. Statistical tests (**l** and **m**, sign of the mean): $^{***}P < 10^{-4}$. In **j**, $P = 0.73 \pm 0.008$. In **h**–**l**, $N = 3$ biological repeats with $n = 12$ doublets. 2D, two dimensional.

shows cluster movements, with typical cluster velocities around 0.1–1 µm min^{-1}.

To quantify the cortical myosin distribution, we defined a polarity vector **p** associated with each cell, which was obtained from the myosin signal intensity on the cell surface, corrected for a gradient in the z direction away from the microscope objective and for the anisotropy of the point spread function (Extended Data Fig. 5c–e and Supplementary Section 5.2). In line with our observation of myosin clusters, the two cell polarity vectors were consistently pointing away from the axis joining the doublet at an angle of nearly 90°, in opposite directions in each cell of the doublet (Fig. 3h–k). The cortical myosin polarity axis was correlated with both the doublet rotation axis and the orientation of the yin–yang interface deformation (Fig. 3l,m). To better visualize the distribution of cortical myosin, we averaged the myosin intensity profile in a reference frame defined by the rotation vector and the cell doublet axis. This again revealed strong myosin accumulation near the cell–cell interface, away from the direction of cell motion (Fig. 3n and Extended Data Fig. 7). In contrast, we find that single cells that do not undergo rotation exhibit a polarized myosin distribution that is fixed in time (Extended Data Fig. 1b,c and Supplementary Section 6). Overall, we conclude that the cortical myosin accumulates in clusters whose positions are correlated with rotation and interface deformation (Fig. 3o).

An active surface model recapitulates doublet rotation

We then wondered if we could understand how doublets were physically rotating and the complex shape of their cell–cell interfaces (Fig. 4a and Extended Data Fig. 8). We considered a physical model where each cell is described as an active viscous surface, subjected to active tension (Supplementary Section 9). Cell–cell adhesion is described by an interaction potential acting between all pairs of cell surface points, with short-range repulsion and intermediate-range attraction. Surface flows are obtained from force balance equations at the cell surface, both on the outer interface and at the cell–cell contact, taking into account an external friction force proportional to the cell surface velocity. Polarity vectors were assigned to each cell, opposite to each other and oriented with a constant angle away from the axis joining the cells. A profile of active tension was imposed around the cell polarity axis (Supplementary Section 9.3). This profile was set using measurements of cortical myosin intensity in a reference frame defined by the cell polarity vector and the axis joining the doublet cells (Fig. 4b,c and Extended Data Figs. 7 and 8a,c). Simulations were performed using the Interacting Active Surfaces (IAS) numerical framework[20] (Fig. 4d and Supplementary Sections 9.1 and 9.2). Solving for the doublet dynamics, we found that a cortical flow emerges, the cell doublet rotates, and the cell–cell interface acquires a deformed shape (Fig. 4e, Extended Data Fig. 8f and Supplementary Video 11). The simulated interface shape was a pure yin–yang deformation correlated with the direction of rotation (Fig. 4e,f), the doublet was elongated, and the major axis of elongation was rotating with the doublet (Fig. 4g), as observed experimentally (Fig. 2c,h). Other deformation modes were however absent, in contrast to experiments (Figs. 2g and 4f). Both the simulated rotational velocity and the magnitude of the interface deformation increase with the magnitude of the active tension modulation (Fig. 4h,i and Supplementary

Fig. 4 | Interacting active surface simulations of a rotating doublet. **a**, A schematic of doublet rotation. **b**, A map of the average normalized experimental myosin intensity, in spherical coordinates around a reference frame defined in schematics (right). **c**, Profiles of myosin intensity as a function of the angle θ defined in **b**, showing the time-average profile of individual cells (grey), the profile averaged over all cells (blue) and the fitted profile (red). **d**, A schematics for the IAS simulation of a rotating doublet. **e**, IAS simulation results (where η is the cortical viscosity and γ_a is the reference active tension). Time (t) is relative to the beginning of Supplementary Video 11. **f**, The amplitude of the mode deformation for the simulated cell–cell interface in **e**. **g**, The correlation of the yin–yang mode orientation and the doublet principal elongation axis with the direction of rotation. **h**, Left: the rotation velocity of the simulated doublet as a function of the relative active tension modulation $\sigma_\gamma{}^m/\&\#x276C;\gamma^m\&\#x276D;$ ($\eta/\gamma_a = 1$ min). Right: the experimental rotation velocity as a function of the relative myosin variation $\sigma_I/\&\#x276C;I\&\#x276D;$, with the average rotational velocity shown in red. Definitions in Supplementary Section 9.4. **i**, Left: the dimensionless amplitude $\sqrt{H^2_{y-y}}/R$ of the yin–yang deformation mode as a function of the amplitude of the active tension modulation (Supplementary Section 9.4). Right: the experimental amplitude of the yin–yang deformation mode as a function of the myosin variation, including the binned averages (red). **j**, The IAS doublet simulation for cortical myosin profiles consistent with doublets in different symmetry groups (Schoenflies notation on the left). **k**, An example of a rotating doublet displaying a bowl mode deformation of the doublet interface. Top: the maximum projection of the E-cadherin-mNG (green) and myosin-KO1 (grey). Bottom: three-dimensional segmentation of the doublet labelled with normalized myosin intensity. **l**, Left: the correlation of the bowl mode amplitude with the difference of the average rescaled active tensions $\gamma_1{}^m$, $\gamma_2{}^m$. Right: the experimental correlation of the bowl mode amplitude with the difference of the average myosin intensities $\&\#x276C;I_1\&\#x276D;$, $\&\#x276C;I_2\&\#x276D;$. The binned average is shown in red and individual data points in blue. **m**, The experimental histogram of the correlation (right) of the saddle-node mode characterized by tensor Q^{S12} with the difference of the cortical myosin nematic tensors Q^1, Q^2 (see schematics on the left). Red line, mean. Error bars show the 95% confidence interval of the mean. See Supplementary Section 9. $N = 3$ biological repeats; $n = 12$ doublets. Statistical tests (**h**, **i**, **l**: sign of correlation; **m**: sign of the mean): $^{*}P = (1.21 \pm 0.07) \times 10^{-3}$ and $^{***}P < 10^{-4}$.

https://doi.org/10.1038/s41567-024-02460-w

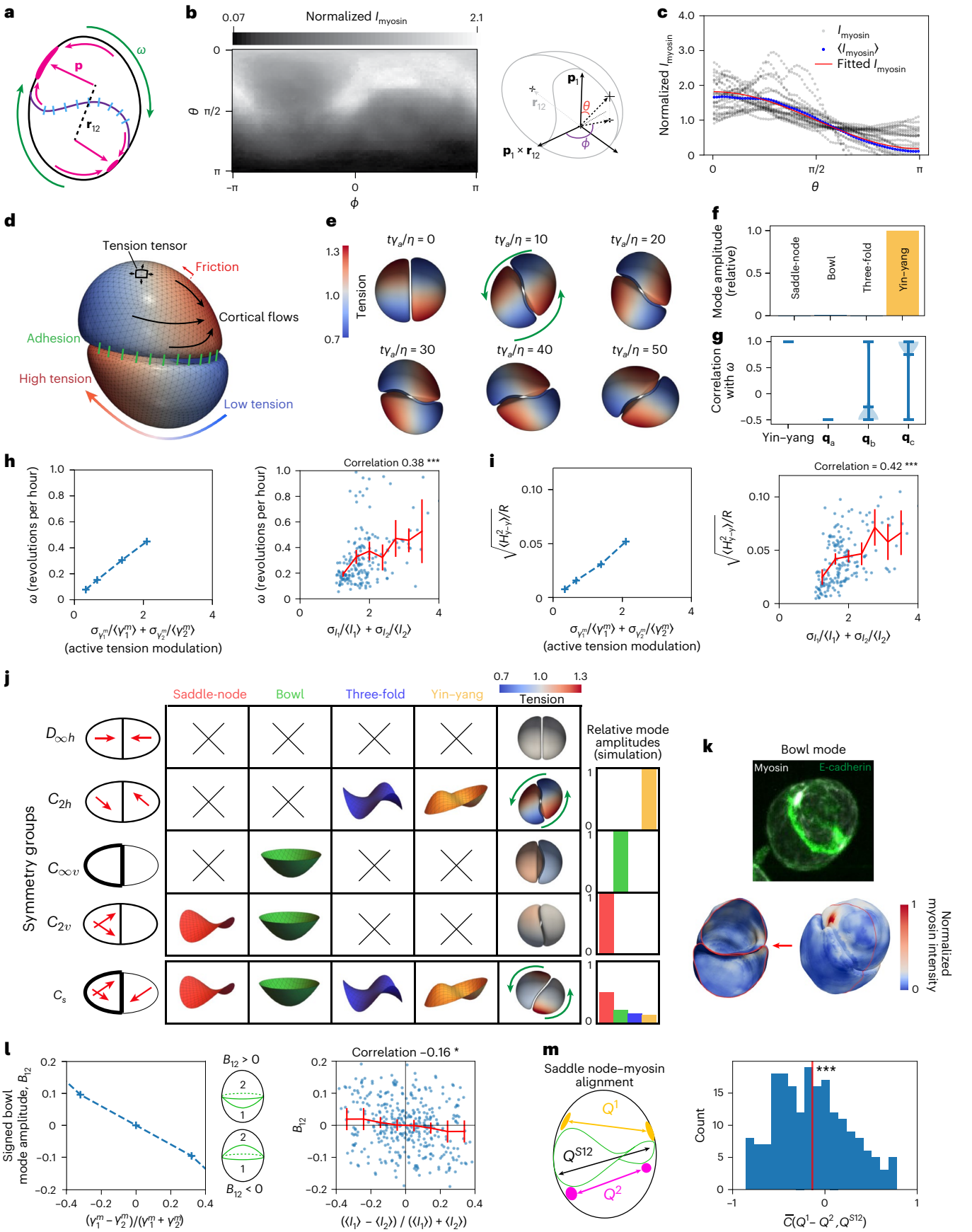

https://doi.org/10.1038/s41567-024-02460-w

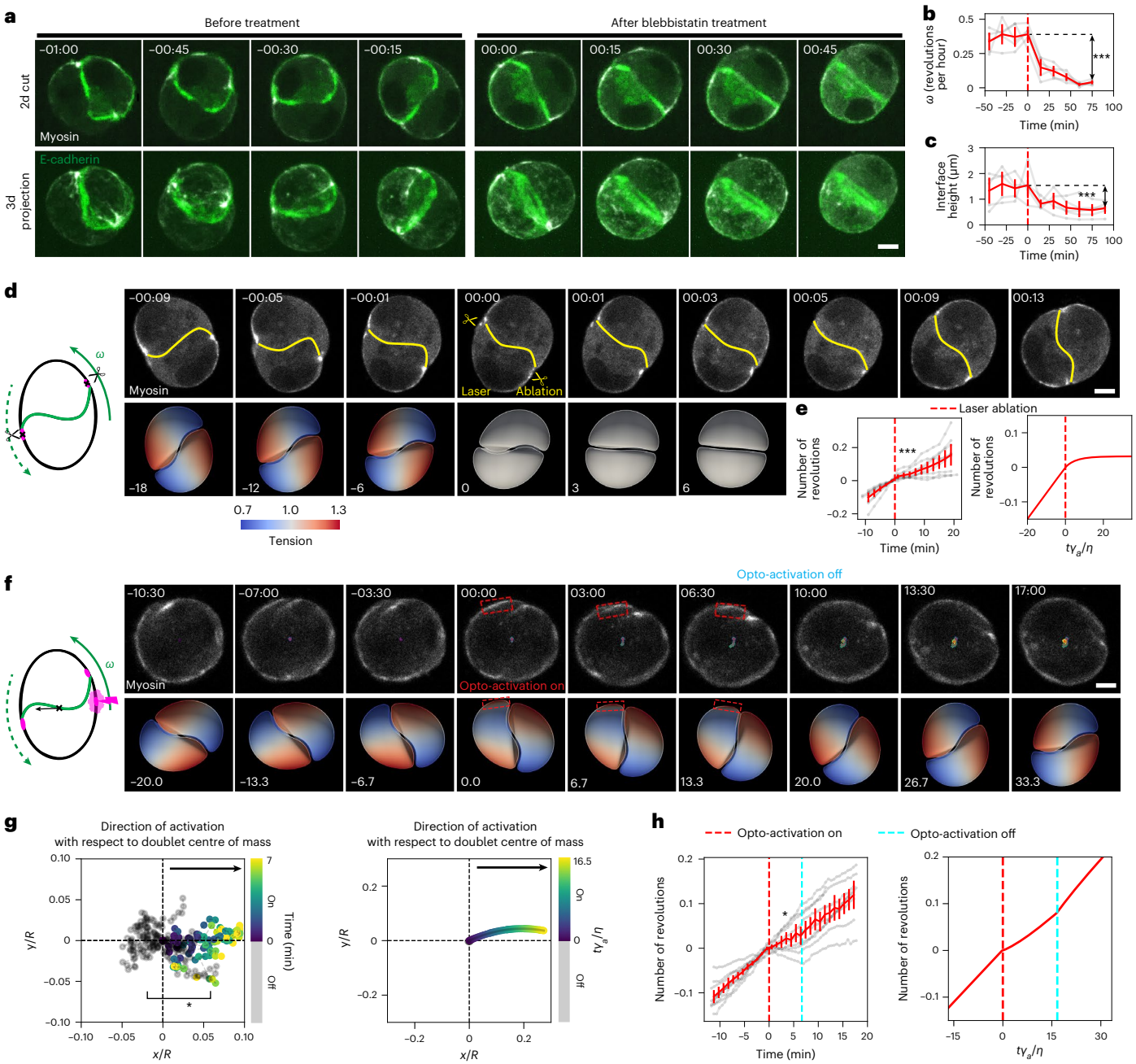

Fig. 5 | Perturbing the rotation motor. a, Snapshots of a rotating doublet before and after Blebbistatin treatment, showing E-cadherin-mNG (green) and MRLC-KO1 (grey) (see also Supplementary Video 12) for a representative example of $n = 16$ doublets. **b**, The magnitude of the rotation as a function of time, before and after treatment with blebbistatin, with $n = 4$ doublets. **c**, The magnitude of the interface height as a function of time, before and after treatment with blebbistatin, with $n = 4$ doublets. Panels **b** and **c** show the doublet shown in **a**, red lines indicate addition of blebbistatin. **d**, Snapshots of a rotating doublet labelled with MRLC-GFP (grey) (top, experiments; bottom, simulation), before and after laser ablation of myosin spots at time 0. In the schematic shown on the left, ablation spots are indicated by two scissors, cells are outlined with black lines and cell–cell junctions are indicated by a green line. See also Supplementary Videos 11 and 12. Representative example of $n = 9$ doublets. **e**, Left: the number of turns as a function of time before and after laser ablation of myosin clusters with $n = 9$ doublets. Right: a similar plot for the simulation in **d**, bottom. The time of ablation is indicated by a dashed red line. **f**, Snapshots of a rotating doublet labelled with MRLC-iRFP (grey), before and after optogenetic activation of RhoA (dashed red rectangle) generating a local myosin cluster (top: experiments; bottom: simulation; activation at time 0) (see also Supplementary Video 15 and 16). In the schematic shown on the left, local Rho activation is indicated by the purple 'lightning' symbol, myosin clusters with a purple dot, cells are outlined by black lines, cell–cell junctions are indicated by a green line and the motion of the centre of mass of the doublet by a black arrow. Representative example of $n = 9$ doublets. **g**, The trajectory of the doublet's centre of mass (normalized by its radius R) before and during optogenetic activation in experiments (left) and in simulations (right) (Supplementary Section 10), computed in the rotating frame and with respect to the activation region localization (experiment, $n = 9$ doublets) and induction of a region of increased active tension in one cell of the doublet (simulation). **h**, The number of visible turns as a function of time, before, during and after optogenetic generation of a myosin cluster (left: experiment, for the doublet shown in **f**; right: simulations). Scale bars: 5 μm. Time in hh:mm in **a** and **d** or mm:ss in **f**. Grey lines in **b**, **c**, **e**, **h**: Individual trajectories. Error bars show the 95% confidence interval of the mean. $N = 3$ biological repeats. Statistical tests: In **b**, the average ω at $t = 75$ min is compared with the average ω for $t \leq 0$ min; In **c**, the average height at $t = 90$ min is compared with the average height for $t \leq 0$ min. P values are $(3.1 \pm 1.4) \times 10^{-5}$ in **e**, $(2.2 \pm 0.1) \times 10^{-3}$ in **g** and $(5.38 \pm 0.14) \times 10^{-3}$ in **h**, and $^{***}P < 10^{-4}$ otherwise (see Supplementary Section 10 for details).

Section 9.4). To test this prediction, we compared the magnitudes of the rotation and the yin–yang interface deformation mode with the variation in the cortical myosin polarity and found that they were indeed correlated (Fig. 4h,i). The simulated rotation magnitude was comparable to experiments for parameters giving rise to cortical flows of ~0.1 μm min^{-1}, comparable to the observed speed of myosin clusters (Extended Data Figs. 4d–h and 8f).

Curie principle applied to doublet interface shape

We then wondered how we could explain the emergence of modes of interface deformation other than the yin–yang shape. We reasoned that the Curie principle, stating that 'the symmetries of the causes are to be found in the effects'[21,22], implies that molecular cues guiding interface deformations should satisfy symmetry rules consistent with the observed interface shape (leaving aside the possibility of spontaneous symmetry breaking). We classified a set of configurations of doublets and polarity axis according to their symmetry properties (Fig. 4j). A configuration where cell polarities are in the same plane but shifted in opposite directions away from the doublet axis belongs to the C_{2h} point group in Schoenflies notation[23]. As a result, such a doublet should exhibit yin–yang and three-fold interface deformation, as observed in simulations (Fig. 4f and Extended Data Fig. 8d). In contrast, tension asymmetry between the two cells of the doublets should give rise to the bowl deformation mode. Meanwhile, a nematic configuration of active tension distribution, with different intensities in each cell, should give rise to the bowl and saddle-node deformation mode (Fig. 4j). Simulating doublets with varying profiles of active tension confirmed these predictions (Fig. 4j). We then verified if this relationship between modes of cortical myosin distribution and modes of interface deformation could be observed in experiments. Indeed, we found that the magnitude of the bowl deformation mode was correlated with the difference in the average cortical myosin intensity of the two doublet cells (Fig. 4k,l). We also noticed that the distribution of cortical myosin had a secondary, less concentrated cluster opposite to the main myosin cluster (Fig. 3n and Extended Data Fig. 7). We reasoned that this secondary cluster was giving rise to a nematic distribution of cortical myosin, quantified by a nematic tensor[24]. Indeed, we measured a negative correlation between the nematic tensor of the saddle-node interface deformation mode and the difference of the cortical myosin nematic tensor between the two doublet cells (Fig. 4m). We then verified that simulating a doublet with an active tension profile summing a polar, nematic distribution and a difference in average tension between the two doublets cells resulted in a complex interface shape with a similar mode decomposition as in experiments (Fig. 4j, last row and Fig. 2g). We conclude that the complex shape of the doublet interface can be understood on the basis of symmetry principles from the cortical myosin distribution in the doublet.

Perturbing myosin clusters affects doublet shape and motion

We then reasoned that, if the myosin clusters are responsible for cell rotation and interface deformation, perturbing their activity and localization would affect the cell doublet shape and motion. Indeed, treatment with the myosin inhibitor blebbistatin (Fig. 5a) resulted in simultaneous rotation arrest, flattening of the interface and disappearance of clusters of phosphorylated myosin (Fig. 5a–c and Extended Data Fig. 9a,b) The effect of the blebbistatin-induced arrest of rotation was reversible. When we washed out the inhibitor, doublets retrieved rotational motion and a bent interface (Extended Data Fig. 9 and Supplementary Video 12). By incubating cells with inhibitors of Rac1 and Arp2/3 (CK666; Methods), which are key regulators of actin polymerization during single cell motility[25,26], we also tested whether actin polymerization was required for the rotation. Doublet rotations were arrested upon treatment but resumed after washing (Extended Data Fig. 10 and Supplementary Videos 13 and 14). This arrest was accompanied by a disassembly of myosin clusters (Extended Data Fig. 10 and Supplementary Videos 13 and 14).

We then aimed at specifically altering the two opposite myosin spots using laser ablation (Fig. 5d). This induced transient arrest of the rotation and interface flattening. Following a lag time of ~10 min, rotation restarted with a simultaneous increase in rotation velocity and interface deformation (Fig. 5e and Supplementary Video 15). Suppressing the gradient of active tension in the simulation also suppressed the rotation (Fig. 5d,e and Supplementary Video 16). To generate additional ectopic local myosin clusters, we then engineered a stable optogenetic cell line that we used to locally activate Rho (Fig. 5f, Supplementary Video 17 and Methods). Transient Rho activation resulted in ectopic myosin activation at the cell cortex comparable in intensity and size to spontaneous myosin clusters. This new cluster triggered the displacement of the doublet away from the region of activation while the doublet kept rotating (Fig. 5f–h). Introducing an ectopic region of increased active tension in simulations resulted in a similar drift of the doublet (Fig. 5f–h and Supplementary Video 18). Altogether, these results support the central role of myosin clusters for driving doublet rotation.

Discussion

Our analysis shows that doublet rotation arises from myosin clusters positioned away from the axis joining the two doublet cells. Therefore, the doublet cell rotation requires cell–cell interactions to trigger the shift of the cell polarity axis. Consistent with this picture, in our experimental setup, single cells do not rotate. It has been reported that, in a bilayered Matrigel, which provides an external polarization axis, single MDCK cells rotate[11]. In this situation, the environment is providing a preferred direction. It would be interesting to track the cortical myosin distribution in cells rotating in these conditions to test whether the polarity-based mechanism we propose also applies in that context.

Which mechanisms result in myosin cluster formation? Clusters could emerge by spontaneous symmetry breaking from an initially symmetric configuration where the cell polarities are pointing towards each other (Fig. 4j). The dynamics of the increase in the rotation magnitude after cell division (Fig. 1f), which resembles an exponential increase followed by saturation, is consistent with such a scenario. The position of myosin clusters could be related to the small and transient protrusions that are sent by each cell beyond the interface at the cortex (Fig. 3f), consistent with a mechanism reported in refs. 27,28. Alternatively, they form in response to cell interface deformation and induce rotation and further cell interface deformation, with the positive feedback loop at the origin of the instability and spontaneous symmetry breaking necessary for rotation. Among the deformation modes we have analysed, the yin–yang mode has the right symmetry property to be coupled to a shift of the two cell polarities away from the doublet axis, which occurs in opposite directions in each cell of the doublet (Fig. 4j). Interestingly, we also observed that, following cell division, a myosin-dense cluster forms at the centre of the doublet interface and then appears to relocate towards the periphery of the contact (Extended Data Fig. 9c and Supplementary Video 19). We note that myosin clusters have also been reported to generate stress in cytokinesis[29]. We also observe that focal contacts are polarized within each cell of the doublet, such that a myosin cluster in one cell is in close vicinity to a region dense in focal contacts within the opposite cell. This organization suggests either a common origin for myosin and focal contact distribution or a polarization mechanism relying on negative feedback between cortical myosin and focal contacts. Possibly, forces resulting from the inhomogeneous distribution of cortical myosin promote adhesion contacts through a reinforcement mechanism[27,28,30,31]. Interestingly, we observed that, although E-cadherin KO doublets were still rotating, inhibition of Arp2/3 or Rac1 stopped the rotation, indicating that Arp2/3 and Rac1 activity are required for force generation by myosin in the cortex or that additional protrusive activity participates to propelling the doublet.

Our study shows that epithelial cell doublets allow to bridge the gap between microscopic players involved in cell motion and collective tissue dynamics. We propose that the spontaneous rotation we observed here is a manifestation of the basic principles of cell interactions, involving cross-talks of cell polarity between neighbouring cells and polarity-oriented mechanical interactions between the cells and their environment. The ubiquity of collective rotations observed in various cell types in vitro suggests that they indeed emerge from generic principles. Analysis of the symmetries, here through the Curie principle, helps in making sense of these complex interactions. It would be interesting to see how basic rules of cell polarity interactions combine with mechanical forces to generate tissue self-organisation beyond collective cell rotation.

Online content

Any methods, additional references, Nature Portfolio reporting summaries, source data, extended data, supplementary information, acknowledgements, peer review information; details of author contributions and competing interests; and statements of data and code availability are available at https://doi.org/10.1038/s41567-024-02460-w.

References

1. Cetera, M. et al. Epithelial rotation promotes the global alignment of contractile actin bundles during *Drosophila* egg chamber elongation. *Nat. Commun.* **5**, 5511 (2014).
2. Founounou, N. et al. Tissue fluidity mediated by adherens junction dynamics promotes planar cell polarity-driven ommatidial rotation. *Nat. Commun.* **12**, 6974 (2021).
3. Chougule, A. et al. The *Drosophila* actin nucleator DAAM is essential for left-right asymmetry. *PLoS Genet.* **16**, e1008758 (2020).
4. Erzberger, A., Jacobo, A., Dasgupta, A. & Hudspeth, A. J. Mechanochemical symmetry breaking during morphogenesis of lateral-line sensory organs. *Nat. Phys.* **16**, 949–957 (2020).
5. Naganathan, S. R., Fürthauer, S., Nishikawa, M., Jülicher, F. & Grill, S. W. Active torque generation by the actomyosin cell cortex drives left–right symmetry breaking. *eLife* **3**, e04165 (2014).
6. Pimpale, L. G., Middelkoop, T. C., Mietke, A. & Grill, S. W. Cell lineage-dependent chiral actomyosin flows drive cellular rearrangements in early *Caenorhabditis elegans* development. *eLife* **9**, e54930 (2020).
7. Brangwynne, C., Huang, S., Parker, K. K. & Ingber, D. E. Symmetry breaking in cultured mammalian cells. *Vitr. Cell. Dev. Biol. Anim.* **36**, 563–565 (2000).
8. Jain, S. et al. The role of single-cell mechanical behaviour and polarity in driving collective cell migration. *Nat. Phys.* **16**, 802–809 (2020).
9. Lo Vecchio, S. et al. Spontaneous rotations in epithelia as an interplay between cell polarity and boundaries. *Nat. Phys.* **20**, 322–331 (2024).
10. Fernández, P. A. et al. Surface-tension-induced budding drives alveologenesis in human mammary gland organoids. *Nat. Phys.* **17**, 1130–1136 (2021).
11. Chin, A. S. et al. Epithelial cell chirality revealed by three-dimensional spontaneous rotation. *Proc. Natl Acad. Sci. USA* **115**, 12188–12193 (2018).
12. Leong, F. Y. Physical explanation of coupled cell-cell rotational behavior and interfacial morphology: a particle dynamics model. *Biophys. J.* **105**, 2301–2311 (2013).
13. Camley, B. A. et al. Polarity mechanisms such as contact inhibition of locomotion regulate persistent rotational motion of mammalian cells on micropatterns. *Proc. Natl Acad. Sci. USA* **111**, 14770–14775 (2014).
14. Segerer, F. J., Thüroff, F., Piera Alberola, A., Frey, E. & Rädler, J. O. Emergence and persistence of collective cell migration on small circular micropatterns. *Phys. Rev. Lett.* **114**, 228102 (2015).
15. Thüroff, F., Goychuk, A., Reiter, M. & Frey, E. Bridging the gap between single-cell migration and collective dynamics. *eLife* **8**, e46842 (2019).
16. Li, B., & Sun, S. X. Coherent motions in confluent cell monolayer sheets. *Biophys. J.* **107**, 1532–1541 (2014).
17. Huang, S., Brangwynne, C. P., Parker, K. K. & Ingber, D. E. Symmetry-breaking in mammalian cell cohort migration during tissue pattern formation: role of random-walk persistence. *Cell Motil. Cytoskeleton* **61**, 201–213 (2005).
18. Balasubramaniam, L. et al. Investigating the nature of active forces in tissues reveals how contractile cells can form extensile monolayers. *Nat. Mater.* **20**, 1156–1166 (2021).
19. Tanner, K., Mori, H., Mroue, R., Bruni-Cardoso, A. & Bissell, M. J. Coherent angular motion in the establishment of multicellular architecture of glandular tissues. *Proc. Natl Acad. Sci. USA* **109**, 1973–1978 (2012).
20. Torres-Sánchez, A., Kerr Winter, M. & Salbreux, G. Interacting active surfaces: a model for three-dimensional cell aggregates.*PLoS Comput. Biol.* **18**, e1010762 (2022).
21. Curie, P. Sur la symétrie dans les phénomènes physiques, symétrie d'un champ électrique et d'un champ magnétique. *J. Phys. Theor. Appl.* **3**, 393–415 (1894).
22. Prost, J., Chauwin, J.-F., Peliti, L. & Ajdari, A. Asymmetric pumping of particles. *Phys. Rev. Lett.* **72**, 2652–2655 (1994).
23. Symmetry resources. *Otterbein University* https://symotter.org/ (2021).
24. de Gennes, P. G., Prost, J. & Pelcovits, R. The physics of liquid crystals. *Phys. Today* **48**, 70–71 (1995).
25. Pollard, T. D. & Borisy, G. G. Cellular motility driven by assembly and disassembly of actin filaments. *Cell* **112**, 453–465 (2003).
26. Schaks, M., Giannone, G. & Rottner, K. Actin dynamics in cell migration. *Essays Biochem.* **63**, 483–495 (2019).
27. Brevier, J., Vallade, M. & Riveline, D. Force–extension relationship of cell–cell contacts. *Phys. Rev. Lett.* **98**, 268101 (2007).
28. Brevier, J., Montero, D., Svitkina, T. & Riveline, D. The asymmetric self-assembly mechanism of adherens junctions: a cellular push–pull unit. *Phys. Biol.* **5**, 016005 (2008).
29. Wollrab, V., Thiagarajan, R., Wald, A., Kruse, K. & Riveline, D. Still and rotating myosin clusters determine cytokinetic ring constriction. *Nat. Commun.* **7**, 11860 (2016).
30. Riveline, D. et al. Focal contacts as mechanosensors. *J. Cell Biol.* **153**, 1175–1186 (2001).
31. Balaban, N. Q. et al. Force and focal adhesion assembly: a close relationship studied using elastic micropatterned substrates. *Nat. Cell Biol.* **3**, 466–472 (2001).

Methods

Cell culture and cell lines

Cells were maintained at 37 °C in a 5% CO_2 incubator. All following steps are performed under a sterile hood.

The maintenance of MDCK II cell lines was done using high Glutamax modified Eagle's medium (ref. 41090-028; Gibco), 5% v/v foetal bovine serum (ref. 10270106; South America Gibco), 1% v/v non-essential amino acid (ref. 11140-050; Gibco), 1% v/v sodium pyruvate (ref. 11360-039; Gibco) and 1% penicillin–streptomycin. MDCK cells were replated every 3–4 days when they reached 70–95% confluency. Trypsin-EDTA was used to detach the cells from the plate and with a seeding density of 5×10^4 cm^{-2}. To generate doublets, single cells were embedded in a Matrigel close to the surface. Coverslips were activated by O_2 plasma, and 100% Matrigel (356231; Corning BV) was then used to coat coverslips. Following a 10 min incubation at 37 °C, 100% Matrigel was polymerized and formed a basal layer. Single cells were deposited at a density of 15,000 cells cm^{-2}. After 10 min of incubation, unattached cells and excess medium were removed. Next a drop of 10 µl 100% Matrigel was deposited. After polymerization of Matrigel at 37 °C in the incubator, culture medium was further added. For doublets with distinct cells, cells were centrifuged into micro-cavities, and their diameters were adapted to contain two cells[32]. By default, sister cells are used for representation unless indicated.

We prepared the following stable cell lines: MDCK II E-cadherin-GFP/Podocalyxin-mScarlett/Halo-CAAX was used to visualize the cell–cell junction and the lumen. To generate new myosin clusters by opto-genetics, we prepared a stable MDCK II cell line expressing iLID-LARG::mVenus[33], engineered to be membrane-anchored by a slowly diffusing Stargazin membrane anchor[34] combined with the DH/PH domain of the Leukemia-associated RhoGEF (LARG)[35]. This cell line allowed us to activate Rho locally and trigger the local recruitment of myosin. We visualized Rho activity with an active Rho sensor (2xrGBD-dTomato) and myosin localization with MRLC-iRFP703. We also used the following cell lines: MDCK II VASP-GFP for tracking focal contacts[36], MDCK II MRLC-KO1/E-cadherin-mNG to follow myosin and cell–cell junctions[37], MDCK II MRLC-GFP[38], MDCK II E-cadherin-GFP, MDCK II E-cadherin-DsRed[39], MDCK II Actin-GFP (Nelson laboratory) and MDCK II Lifeact-iRFP. These cell lines allowed us to track specific correlations between rotation and adhesion or cytoskeleton protein localizations. E-cadherin was also used for segmentation purposes. MDCK II E-cadherin-KO[18] was used to study the role of adherens junction in rotating doublet. To visualize F-actin live, we also used SiR-Actin (500 nM, Tebu-Bio, 251SC001). Each experimental condition (biological repeat, denoted by N) was reproduced at least three times on at least ten doublets (denoted by n in captions).

Drug treatments and immuno-fluorescence staining

To investigate the role of myosin, we used blebbistatin (Sigma, B0560) to inhibit myosin with the following steps. Timelapses of samples were acquired under the microscope, and the medium was then changed by a medium containing 10 µM of blebbistatin. Following 1 h incubation, samples were washed three times with fresh medium. Samples were further imaged to visualize the eventual re-initiation of rotation.

To study the role of actin, the Arp2/3 inhibitor (CK-666, SML0006; Sigma) and Rac1 inhibitor (Z62954982; Merck Millipore) were used to interfere with actin dynamics[8]. Drug assays were performed following this protocol: for 30 min doublet dynamics were recorded before drug treatment, then 50 µM CK-666 or 50 µM Rac1 inhibitors were incubated during 30 min. The doublet dynamics were recorded for 2 h after washout.

For immunostaining[9], samples were washed with PBS and then fixed with 4% paraformaldehyde (PFA) diluted in PBS for 15 min. To permeabilize cells, cells were incubated with 0.5% Triton-X-100 for 15 min and then a blocking solution made of 1% normal goat serum in PBS 1× was added overnight. The primary antibody was added directly to the blocking solution for 2 days at 4 °C. Following three washing steps, samples were stained with the relevant secondary antibodies for 2 h at room temperature. We used the following primary antibodies: Anti-E-cadherin (Ab11512; Abcam), Anti-Phospho-Myosin Light Chain 2 (#3674; Cell Signaling Technology), Anti-Paxillin (Ab32084; Abcam) and Alexa FluorTM Phalloidin 488 (A12379; Thermo Fisher) to visualize F-actin. Samples were washed three times in PBS and mounted on a home-made sample holder system for imaging and conservation.

Microscopy

High-throughput imaging was done using a spinning disk microscope with an inverted Leica spinning disk DMI8 equipped with an Orca Flash 2.0 camera (2,048 × 2,018 pixels with a size of 6.5 µm) using a 63× glycerol objective (numerical aperture of 1.3). The microscope was equipped with an incubation chamber to maintain the samples at 37 °C, 5% CO_2 and 85% humidity conditions.

To record the initiation of rotation, MDCK doublets were imaged for 5 h after cell seeding. Three-dimensional stacks were acquired with a z step of 1 µm and x–y resolution of 0.206 or 0.103 µm, every 10 min up to 12 h.

Confocal imaging of fixed samples was performed using the same setup. Laser power and digital gain settings were unchanged within a given session to ease quantitative comparison of expression levels among doublets.

We locally activated Rho with the scanning head of a confocal microscope (Leica SP8-UV) with a 458 nm laser each 10 s for 20 min, taking an image every minute. We could follow RhoA activity with a Rho binding domain sensor for active Rho (2xrGBD::dTomato)[40] and myosin with the MRLC::iRFP703 probe.

Image analysis

Three-dimensional segmentation of cells was performed using a custom-written ImageJ macro involving the LimeSeg plugin[41] (Supplementary Section 1). The centre of mass and surfaces of cells were computed from the segmented three-dimensional (3D) meshes using a written Python code. For the velocity measurements, rotational velocity of cells was computed using the cell-to-cell centre of mass vector, the velocity of cell 1 and the velocity of cell 2 (Supplementary Section 2).

Segmentation of the interface was performed using a customized Python code from the 3D meshes of each cell in a doublet. The 3D point cloud of the interface was then fitted to a polynomial function of degree three. Characterization of the interface deformation and shape was then performed on the fitted surface (Supplementary Section 4).

The fluorescence intensity signal of myosin was extracted from images and attributed to vertices of 3D meshes. The myosin distribution was then characterized by a polarity vector and a nematic tensor. We correlated these descriptors to the interface shape and the doublet rotation (Supplementary Section 5).

Planar projections of the basal (E-cadherin) signal were created using a custom Python code (Supplementary Section 7).

For the visualization and 3D rendering, we used Paraview[42] software.

IAS simulation framework

Simulations of rotating doublets were performed using the IAS framework. A polarity is introduced for each cell, which modulates the active tension profile along its surface. This leads to the emergence of a cortical flow that propels the cells through friction with the external medium. The integrity of the doublet is maintained using an adhesion interaction potential. See Supplementary Section 9 for a complete description of the simulations and parameters used.

Statistical tests and data visualization

We used a bootstrapping approach for all statistical tests performed[43]. Given N observed quantities $(x_1, x_2, \ldots, x_N)$, we compute an estimate

$F(\{x_i\})$ of an underlying parameter of interest f. F can be the sample mean (Figs. 2c,h, 3l,m, 4m, 5b,c,e,g,h and Extended Data Fig. 5e), a correlation coefficient (Fig. 4h,i,l) or another estimate (Fig. 3j and Supplementary Section 5.4). Using random sampling with replacement, we generate n samples and construct a probability distribution B_n that approximates the distribution of the true value of f given the observed data $(x_1, x_2, \ldots, x_N)$. The P values of all the tests are then generated using B_n. For instance, the P value P_n associated to the hypothesis that f is positive is the probability $P_{B_n}(F<0)$ (see ref. 43, chapter 15.4). Since P_n is obtained by dividing the number of bootstrap samples $\{x_i^*\}$ for which $F(\{x_i^*\})<0$ by the total number of samples n, lower P values require more samples to be accurately computed. In particular, given an asymptotic P value $P_\infty>0$, the probability to obtain $P_n=0$ with n samples is $(1-P_\infty)^n$, which is equal to 0.67% with $P_\infty=10^{-4}$ and $n=50{,}000$ samples. We therefore performed the tests in Figs. 2c,h, 3l,m, 4h,i,m, 5b,c and Extended Data Fig. 5e (λ_z) with 50,000 samples, and since we obtained $P_n=0$, we inferred that $P<10^{-4}$. For Figs. 3j, 4l, 5e,g,h and Extended Data Fig. 5e (λ_x, λ_y), we provide 95% confidence intervals for the P values, obtained from 10 replicates of 50,000 (1,000 in Fig. 3j and Extended Data Fig. 5e) bootstrap samples. For the correlation tests in Fig. 4h,i,l, we generated independent samples of the correlation defined as $\langle(a-\langle a\rangle)(b-\langle b\rangle)\rangle/(\sigma_a\sigma_b)$ (for two signals a and b with respective standard deviations of σ_a and σ_b). This correlation takes values between −1 and 1.

Violin plots are used in Figs. 2c,h and 4g to visualize statistical distributions. There, the central line corresponds to the mean while the extremum lines correspond to the minimum and maximum of the distribution.

Reporting summary

Further information on research design is available in the Nature Portfolio Reporting Summary linked to this article.

Data availability

All experimental data can be provided upon request to D.R.

Code availability

The custom C++ and python codes used in this study are available in the GitHub online repository at https://github.com/QVbb8/doublet-rotation[44].

References

32. Bhat, A. et al. How to orient cells in microcavities for high resolution imaging of cytokinesis and lumen formation. *Methods Cell Biol.* **158**, 25–41 (2020).
33. Guntas, G. et al. Engineering an improved light-induced dimer (iLID) for controlling the localization and activity of signaling proteins. *Proc. Natl Acad. Sci. USA* **112**, 112–117 (2015).
34. Natwick, D. E. & Collins, S. R. Optimized iLID membrane anchors for local optogenetic protein recruitment. *ACS Synth. Biol.* **10**, 1009–1023 (2021).
35. Martz, M. K., Grabocka, E., Beeharry, N., Yen, T. J. & Wedegaertner, P. B. Leukemia-associated RhoGEF (LARG) is a novel RhoGEF in cytokinesis and required for the proper completion of abscission. *MBoC* **24**, 2785–2794 (2013).
36. Lo Vecchio, S. et al. Collective dynamics of focal adhesions regulate direction of cell motion. *Cell Syst.* **10**, 535–542.e4 (2020).
37. Bhat, A. *Myosin Cluster Dynamics and Their Roles in Epithelial Wound Ring Constriction*. PhD dissertation, Strasbourg Univ. (2019).
38. Watanabe, T., Hosoya, H. & Yonemura, S. Regulation of myosin II dynamics by phosphorylation and dephosphorylation of its light chain in epithelial Cells. *MBoC* **18**, 605–616 (2007).
39. Adams, C. L., Chen, Y.-T., Smith, S. J. & James Nelson, W. Mechanisms of epithelial cell–cell adhesion and cell compaction revealed by high-resolution tracking of E-cadherin–green fluorescent protein. *J. Cell Biol.* **142**, 1105–1119 (1998).
40. Mahlandt, E. K. et al. Visualizing endogenous Rho activity with an improved localization-based, genetically encoded biosensor. *J. Cell Sci.* **134**, jcs258823 (2021).
41. Machado, S., Mercier, V. & Chiaruttini, N. LimeSeg: a coarse-grained lipid membrane simulation for 3D image segmentation. *BMC Bioinform.* **20**, 2 (2019).
42. Ahrens, J., Geveci, B. & Law, C. in *Visualization Handbook* (eds Hansen, C. D. & and Johnson, C. R.) 717–731 (Elsevier, 2005).
43. Efron, B. & Tibshirani, R. J. *An Introduction to the Bootstrap* (Chapman and Hall/CRC, 1994).
44. Vagne, Q. doublet-rotation. *GitHub* https://github.com/QVbb8/doublet-rotation (2024).

Acknowledgements

We thank E. Grandgirard and the Imaging Platform of IGBMC, and the Salbreux and Riveline groups for help and discussions. Q.V. and G.S. are supported by the University of Geneva. L.L. and T.G. are supported by HFSP and by the University of Strasbourg and by la Fondation pour la Recherche Médicale. A.T.S. was supported by the European Molecular Biology Laboratory (EMBL). J.V.U. was supported by funding from the European Union's Horizon 2020 research and innovation programme under Marie Skłodowska-Curie grant agreement no. 747242. D.R. acknowledges the Interdisciplinary Thematic Institute IMCBio, part of the ITI 2021–2028 programme of the University of Strasbourg, CNRS and Inserm, which was supported by IdEx Unistra (ANR-10-IDEX-0002), and by SFRI-STRAT'US project (ANR 20-SFRI-0012) and EUR IMCBio (ANR-17-EURE-0023) under the framework of the French Investments for the Future Program. O.P. and D.R. acknowledge funding from Swiss National Science Sinergia grant CRSII5_183550. D.R. and A.H. acknowledge the Research Grant from Human Frontier Science Program (ref. no. RGP0050/2018).

Author contributions

G.S. and D.R. supervised the study. L.L., T.G. and D.R. conceived and analysed experiments. L.L. performed the experiments with support from T.G., R.B. and M.L. O.P. and K.v.U. contributed the new optogenetic tool, and C.M.-L. and A.H. contributed cell lines. T.G., Q.V. and G.S. performed data analysis. Q.V. and G.S. designed the theoretical model. Simulations were performed by Q.V. with support from A.T.-S. The manuscript was written by G.S. and D.R. on the basis of joint discussions with L.L., T.G. and Q.V.

Competing interests

The authors declare no competing interests.

Additional information

Extended data is available for this paper at https://doi.org/10.1038/s41567-024-02460-w.

Supplementary information The online version contains supplementary material available at https://doi.org/10.1038/s41567-024-02460-w.

Correspondence and requests for materials should be addressed to Daniel Riveline or Guillaume Salbreux.

Peer review information *Nature Physics* thanks Mingming Wu and the other, anonymous, reviewer(s) for their contribution to the peer review of this work.

https://doi.org/10.1038/s41567-024-02460-w

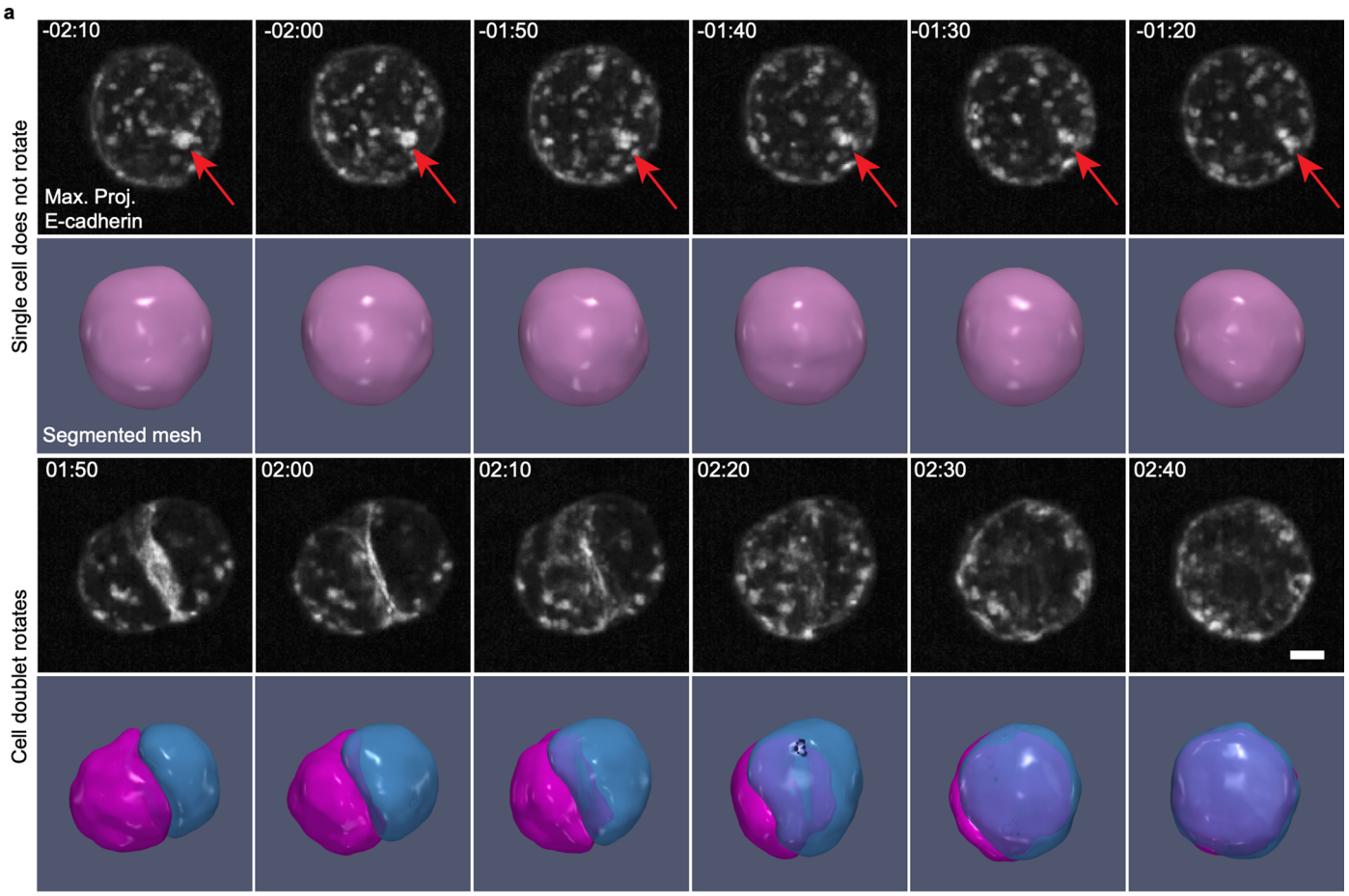

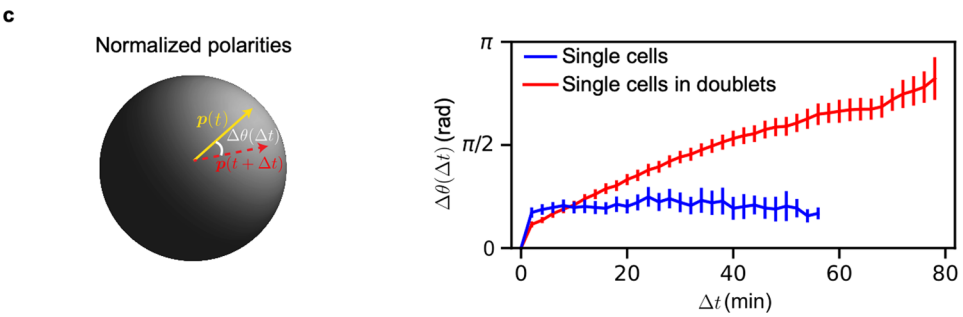

Extended Data Fig. 1 | See next page for caption.

https://doi.org/10.1038/s41567-024-02460-w

Extended Data Fig. 1 | Single cells are polarized but do not rotate. **a**. Snapshot of single cell (two top rows) and cell doublet (two bottom rows). Cells labelled with E-cadherin-mNG (grey) - see beginning of Supplementary Video 2. For each case, top row: maximum projection of E-cadherin, bottom row: cell segmentation. Time relative to cell division. **b**. Snapshots of single cells labelled with MRLC-GFP (grey). Top row: cross-section, bottom row: maximum projection. Representative example of n > 30 cells. **c**. Left: Myosin polarity angles $\Delta\theta$ computed between polarities at t and $t + \Delta t$. Right: Myosin polarity angles as a function of difference of time between frames Δt. Polarity of the single cell is still compared to the polarity of cells in doublets. n = 6 cells in doublets and n > 10 single cells. Scale bars: 5 μm. Time in hh:mm. Error bars: 95% confidence interval of the mean.

https://doi.org/10.1038/s41567-024-02460-w

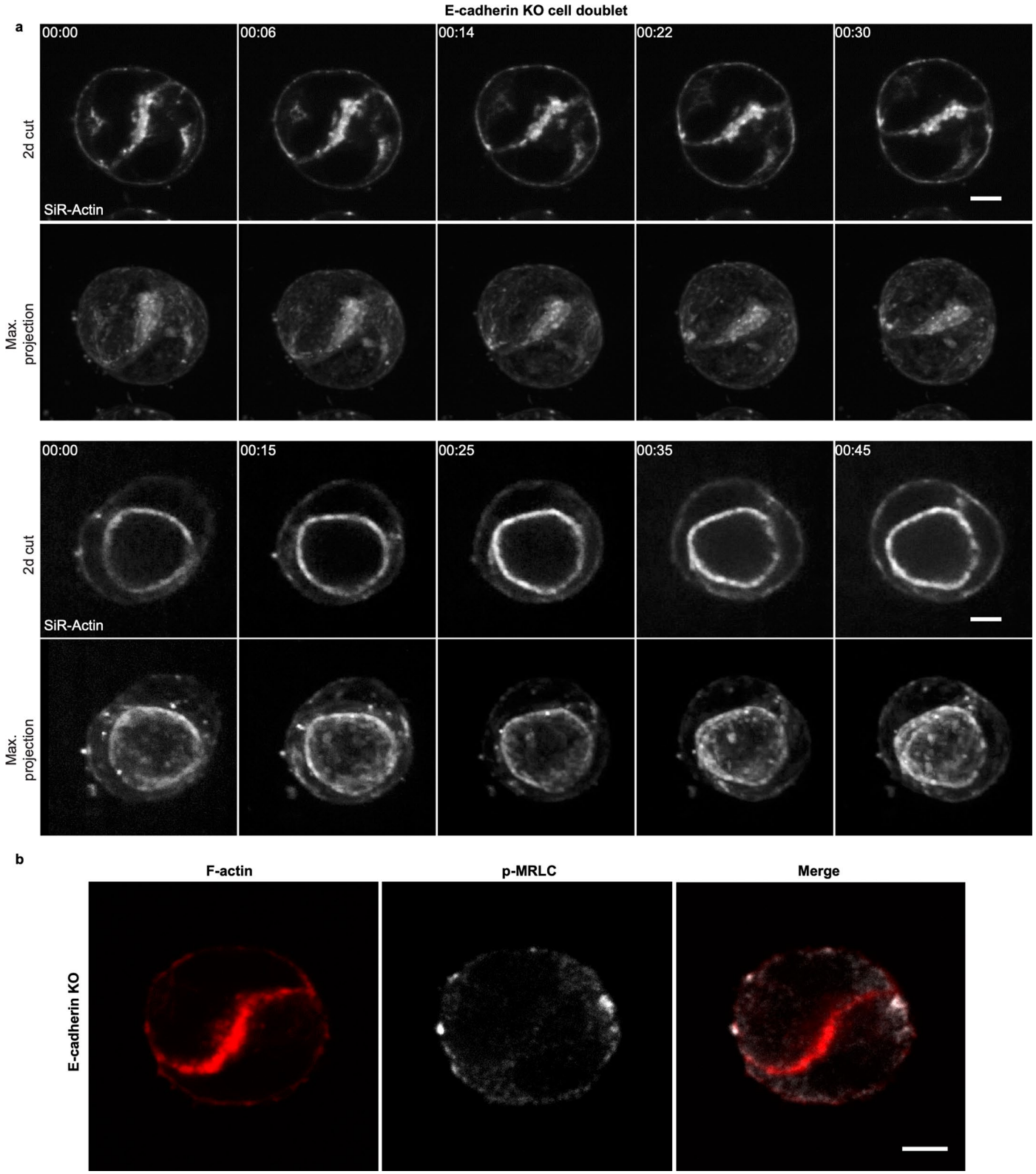

Extended Data Fig. 2 | E-cadherin KO doublet rotates. a. Snapshots of two examples of rotating E-cadherin KO doublets with labelled Sir-Actin in grey (see Supplementary Video 4). Top row: cross-section, bottom row: maximum projection. Representative example of n > 5 doublets. **b**. Snapshots of E-cadherin KO doublet labelled with F-actin (red) and phosphorylated p-MRLC (grey) and merge. Representative example of n > 10 doublets. Scale bars: 5 μm. Time in hh:mm.

https://doi.org/10.1038/s41567-024-02460-w

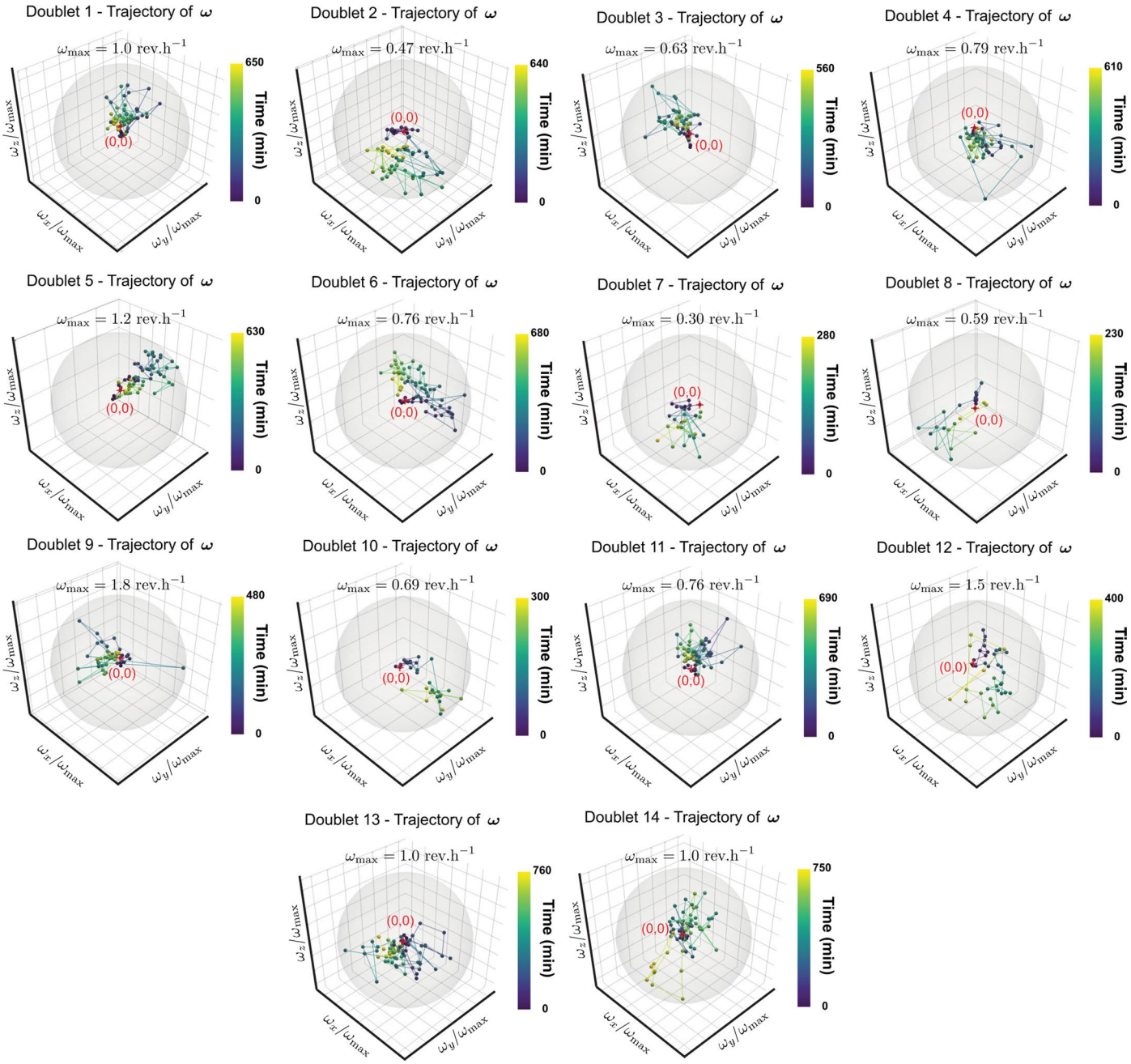

Extended Data Fig. 3 | Trajectories of rotational velocities. Similar to Fig. 1h: trajectories of the rotation vector of cell doublets after cell division for all 14 doublets, normalized with respect to their respective largest amplitudes (corresponding to Supplementary Video 2). Grey sphere has unit radius.

https://doi.org/10.1038/s41567-024-02460-w

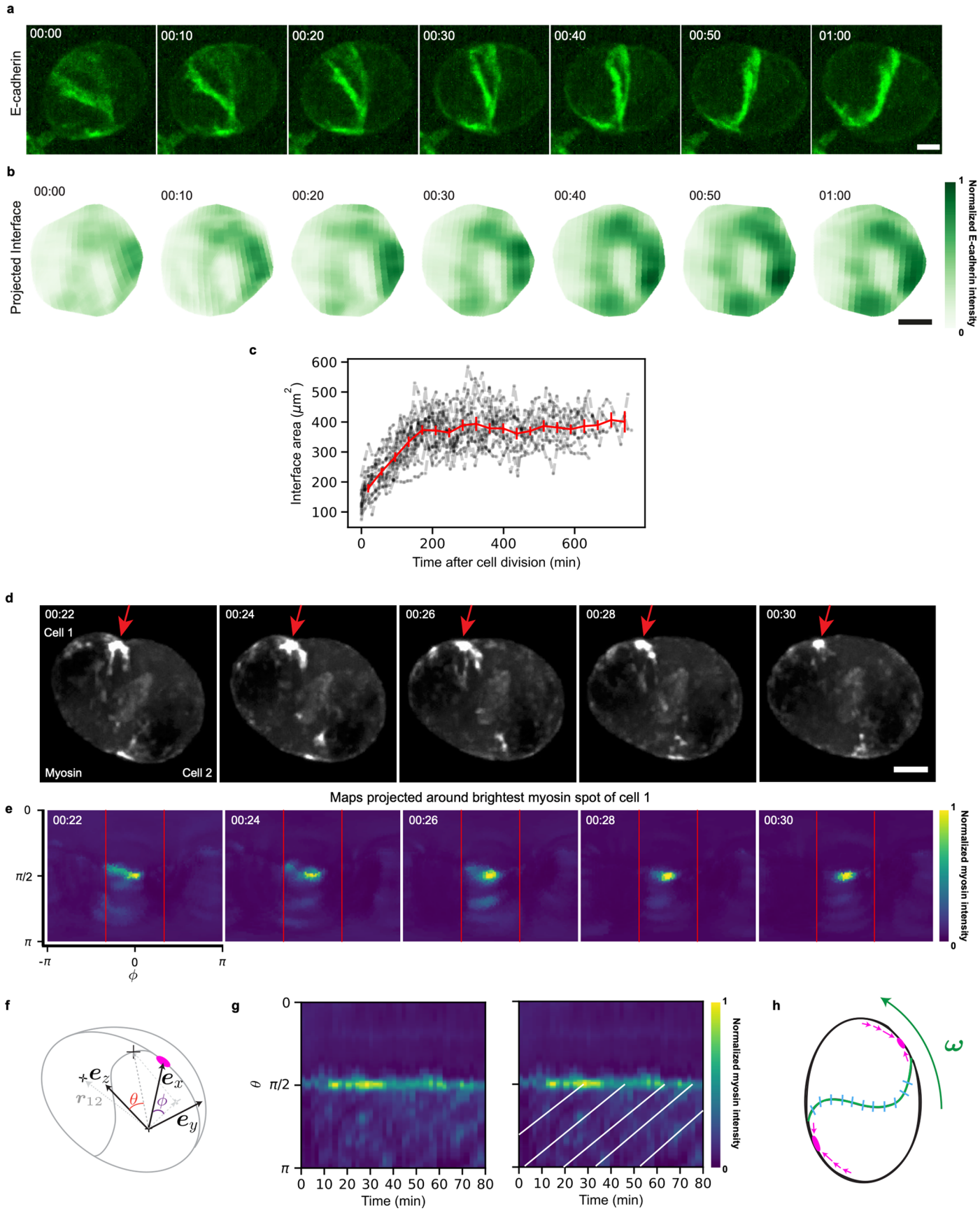

Extended Data Fig. 4 | See next page for caption.

https://doi.org/10.1038/s41567-024-02460-w

Extended Data Fig. 4 | Patterns of E-cadherin at the cell-cell interface and myosin dynamics at the cortex. a. E-cadherin-mNG (grey) labelled rotating doublet. **b**. Patterns of E-cadherin distribution on the doublet cell-cell interface, viewed en-face, for the cell shown in a. **c**. Interface area as a function of time after cell division. n = 14 doublets. **d-e**. Mapping of the myosin dynamics at the cortex (procedure described in Supplementary Information section 8). Myosin clusters exhibit a motion towards red arrows (see Supplementary Video 8). **f**. Reference frame used to generate the maps of e. **g**. Left: Kymograph of the average between the red lines of panel e. Right: Similar kymograph with white lines indicating motion of myosin clusters with a velocity of about 0.3 μm/min. **h**. Schematics for myosin clusters motion (purple) and cadherin (blue) distribution. Scale bars: 5 μm. Time in hh:mm.

https://doi.org/10.1038/s41567-024-02460-w

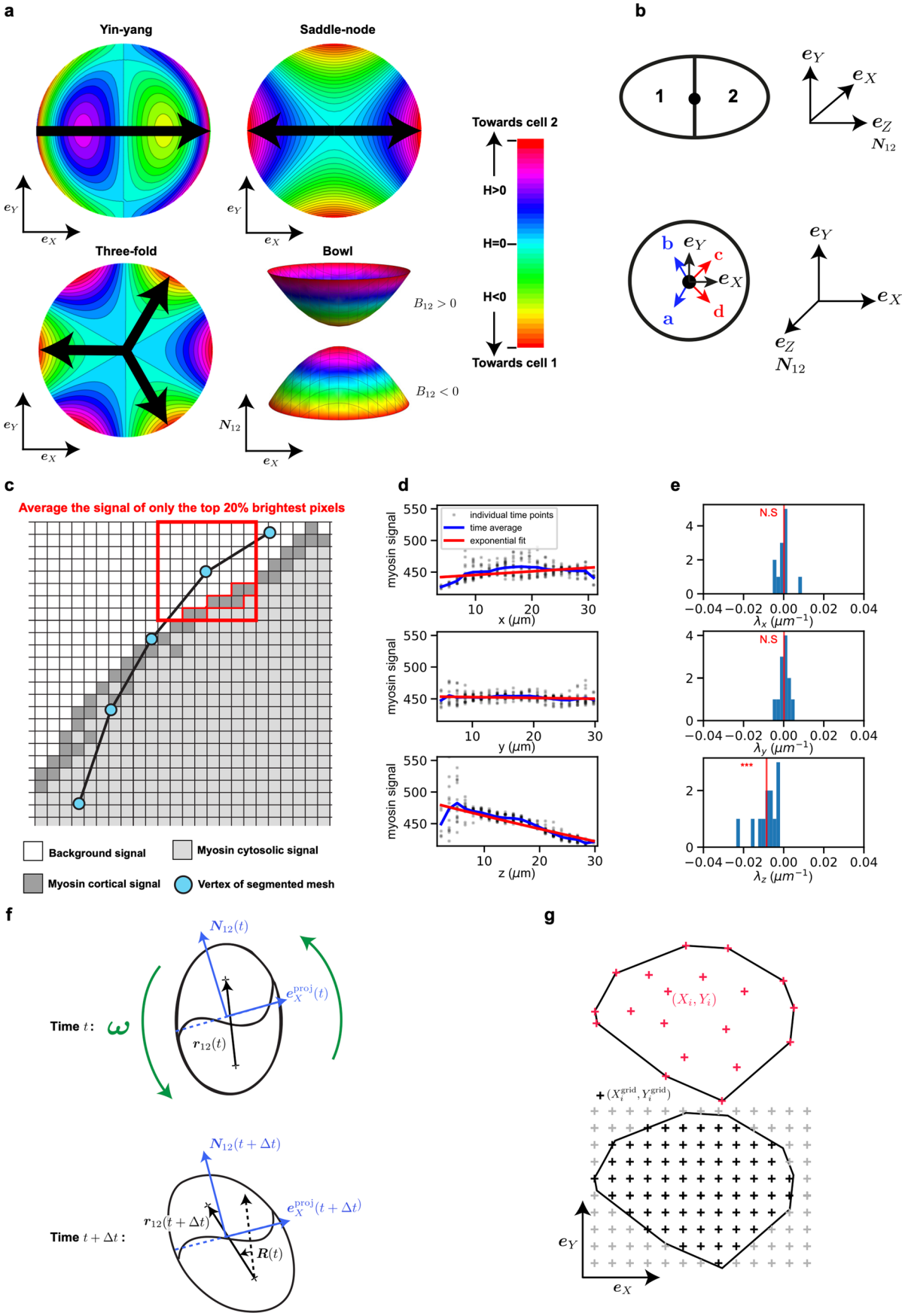

Extended Data Fig. 5 | See next page for caption.

https://doi.org/10.1038/s41567-024-02460-w

Extended Data Fig. 5 | Analysis of interface shape. a. Height profile of interface deformation modes. The yin-yang orientation is characterized by a vector, the saddle-node by a nematic, and the three-fold by a three-fold orientational order. **b**. Schematic for the orientation of the vectors ($\boldsymbol{e}_X$, $\boldsymbol{e}_Y$, $\boldsymbol{e}_Z = \boldsymbol{N}_{12}$) associated to the interface of the cell doublet. The vectors $\boldsymbol{a}$, $\boldsymbol{b}$, $\boldsymbol{c}$, $\boldsymbol{d}$ are introduced to define transformations in Supplementary Table 1. **c**. Schematics of method used to obtain cortical intensities from cell segmentation (see Supplementary Information section 5.1) **d**. Average profile of myosin fluorescence intensity in the x, y, z directions, for a representative doublet. **e**. Histogram of fitting parameters characterizing the average myosin profiles, as in d, for all doublets. Only λ_z is significantly different from 0. **f,g**. Procedure to create interfacial E-cadherin maps shown in Extended Fig. 4b. **f**. A reference vector $\boldsymbol{e}_X^{\mathrm{proj}}$ is rotated with the doublet (using the rotation $\boldsymbol{R}(t)$ of the $\boldsymbol{r}_{12}$ vector) to define a consistent viewpoint and is projected at each time t in the plane of the interface defined by $\boldsymbol{N}_{12}$. **g**. (Top) 2D coordinates (X_i, Y_i) of the interface vertices i, surrounded by their convex hull. (Bottom) A regular grid of new coordinates $(X_i^{\mathrm{grid}}, Y_i^{\mathrm{grid}})$ is created inside the convex hull (black points). Statistical test (sign of the mean): panel e: λ_x: $p = 0.41 \pm 0.01$, λ_y: $p = 0.404 \pm 0.009$, λ_z: ***, $p < 10^{-4}$.

https://doi.org/10.1038/s41567-024-02460-w

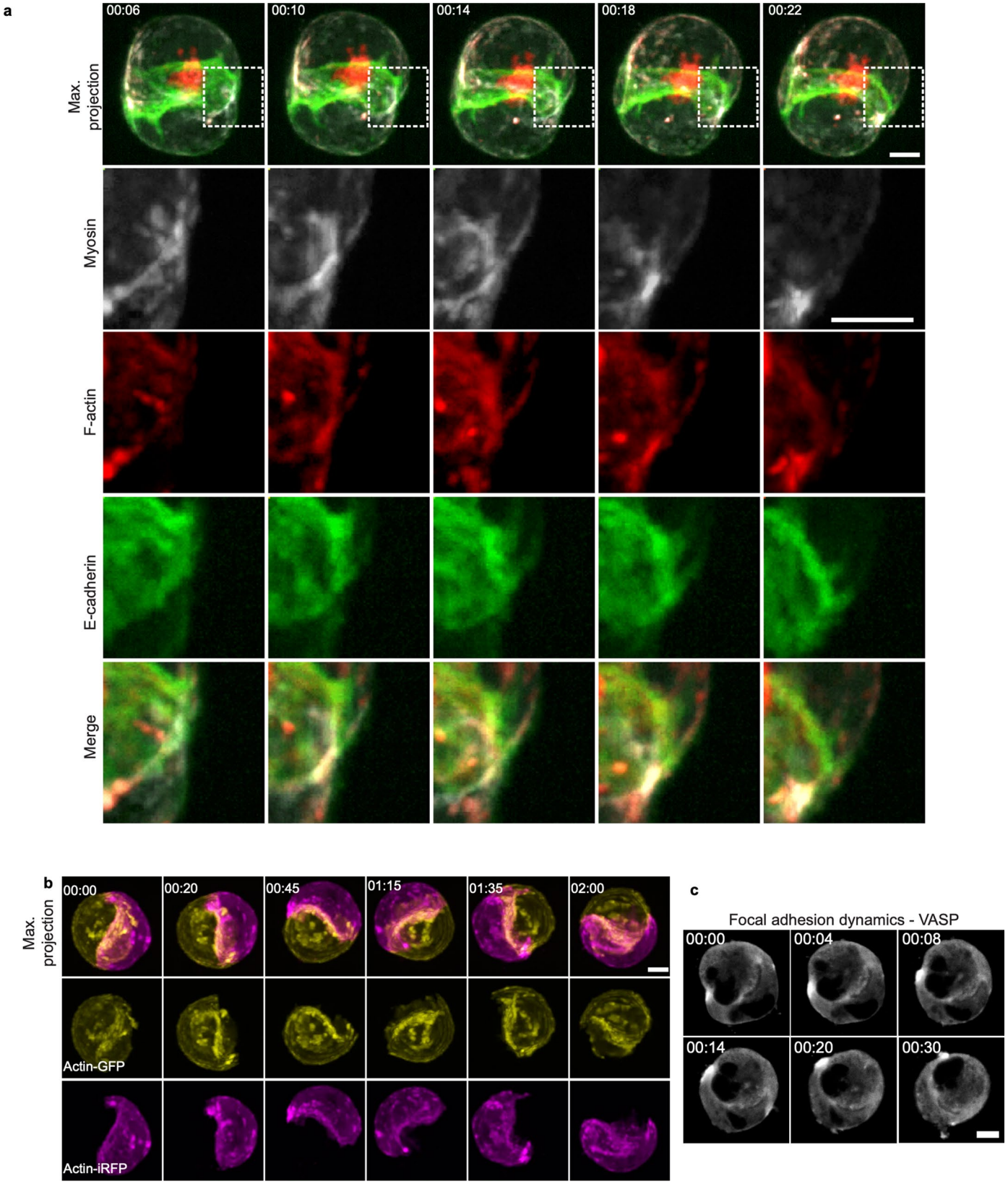

Extended Data Fig. 6 | Dynamics of protrusion, adherens junctions, focal contacts during doublet rotation. a. Snapshots of a rotating doublet with triple label, myosin-KO1 (grey), SiR-Actin (red) and E-cadherin-mNG (green) (see Supplementary Video 10). Representative example of n > 3 doublets. **b**. Snapshot of a rotating doublet with two cells expressing actin of different colours. Labels: Actin-GFP (yellow) and Actin-iRFP (magenta) (see Supplementary Video 9). Representative example of n > 3 doublets. **c**. Dynamics of focal adhesion in the rotating doublet, labelled with VASP-GFP (grey) (see Supplementary Video 7). Scale bars: 5 μm. Time in hh:mm.

https://doi.org/10.1038/s41567-024-02460-w

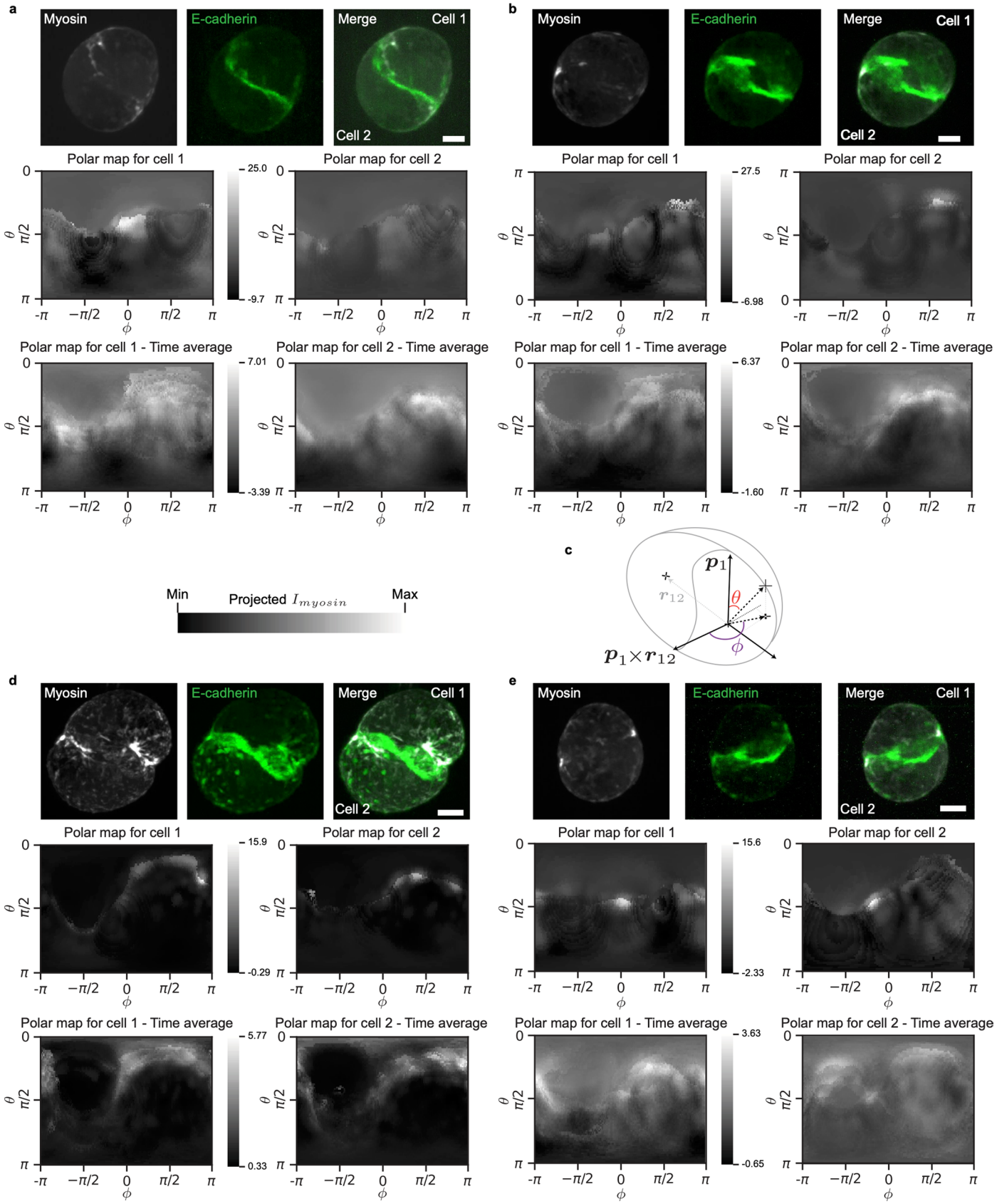

Extended Data Fig. 7 | Example of polar maps of cortical myosin intensity. **a,b,d,e**. Maps of experimental myosin intensity after calibration in spherical coordinates, in a reference frame defined by the polarity axis $\boldsymbol{p}$, the axis of the doublet $\boldsymbol{r}_{12}$ and their cross-product. For each example, top row: snapshot of doublet, maximum projections of myosin (MRLC-GFP), E-cadherin (Ecadherin-mNG) and merge, middle row: individual cell maps corresponding to the above snapshot, bottom row: time average cell maps corresponding to the time series from which the snapshot in the top row was taken from. **c**. Scheme of the reference frame. Scale bar: 5 μm. Procedure described in Supplementary Information section 5.6.

https://doi.org/10.1038/s41567-024-02460-w

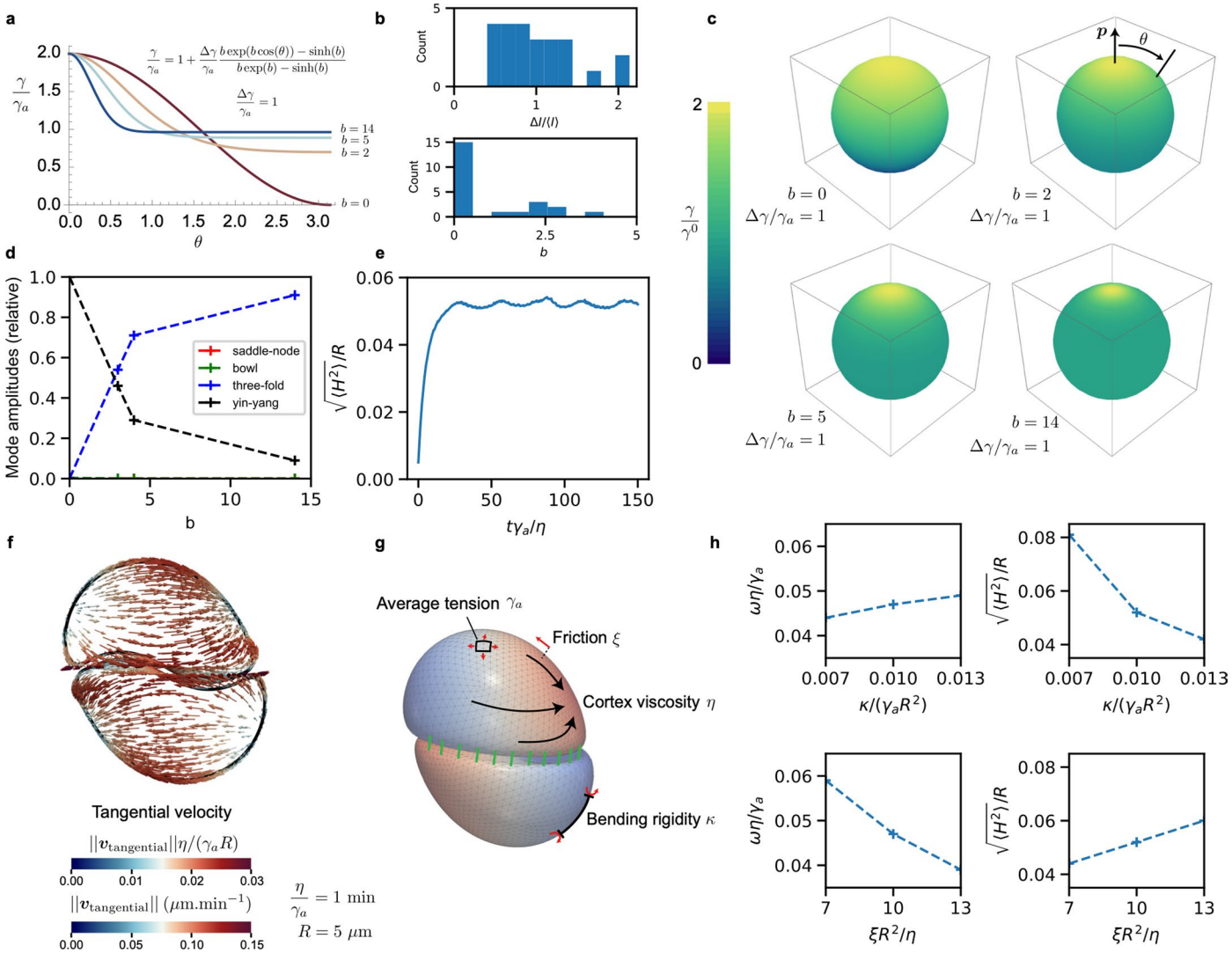

Extended Data Fig. 8 | Additional IAS simulation results. a. Examples of tension profiles around the polarity vector, for different values of the parameter b, which controls the spread of the tension around the maximum value (see Supplementary Information section 9.3). **b**. Histogram of fitted values of b and $\Delta I/\langle I\rangle$ to temporally average myosin profiles for individual doublets, showing the distribution of myosin intensity magnitude and spot sizes. The fitting procedure and parameters are described in Supplementary Information section 9.6. **c**. Tension profiles displayed on spheres with values of b identical to panel a. Larger values of b correspond to smaller spots. **d**. Relative amplitudes of the deformation modes as a function of a varying active tension profile whose spread is determined by b. As the active tension spot size becomes smaller (larger values of b), the yin-yang mode is replaced by the three-fold mode. **e**. Interface deflection as a function of dimensionless time for the simulation shown in Fig. 4e. The interface deflection relaxes to a steady-state showing a slightly oscillatory behaviour. **f**. Cortical flow profile at steady-state for the simulation shown in Fig. 4e. For $\eta/\gamma_a = 1$ min and $R = 5\,\mu$m, the typical flow magnitude is ~0.1μm.min^{-1}. **g**. Explanatory scheme of IAS simulation, with key simulation parameters. **h**. Effect of varying the normalized friction coefficient $\xi R^2/\eta$ and the normalised bending rigidity $\kappa/(\gamma_a R^2)$ on the rotation velocity and the interface deflection, around parameter values chosen in simulations of Figs. 4 and 5 and other panels of Extended Data Fig. 8. See Supplementary Information section 9.5 for additional simulation parameters.

https://doi.org/10.1038/s41567-024-02460-w

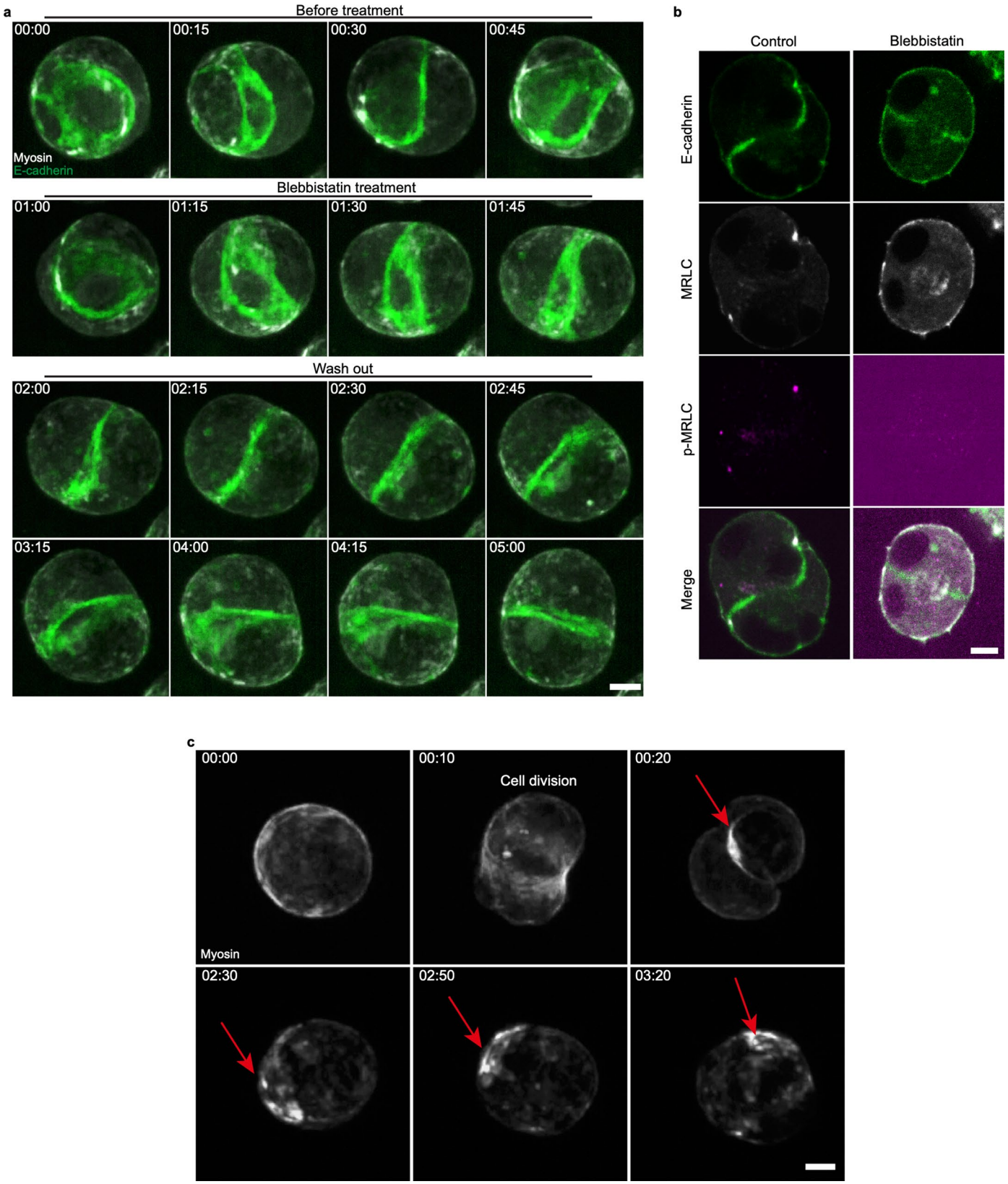

Extended Data Fig. 9 | Blebbistatin treatment, myosin activity and redistribution after cell division. a. Snapshots of experiment before and after blebbistatin treatment followed by washout (see Supplementary Video 12) with E-cadherin in green and myosin in grey. Representative example of n > 5 doublets. **b**. Snapshots of representative examples of distribution of E-cadherin (green), MRLC (grey), phosphorylated p-MRLC (magenta) and merge. n > 10 doublets. **c**. Snapshot of asymmetric myosin distribution before and after cell division (see Supplementary Video 19). Scale bars: 5 μm. Time in hh:mm.

https://doi.org/10.1038/s41567-024-02460-w

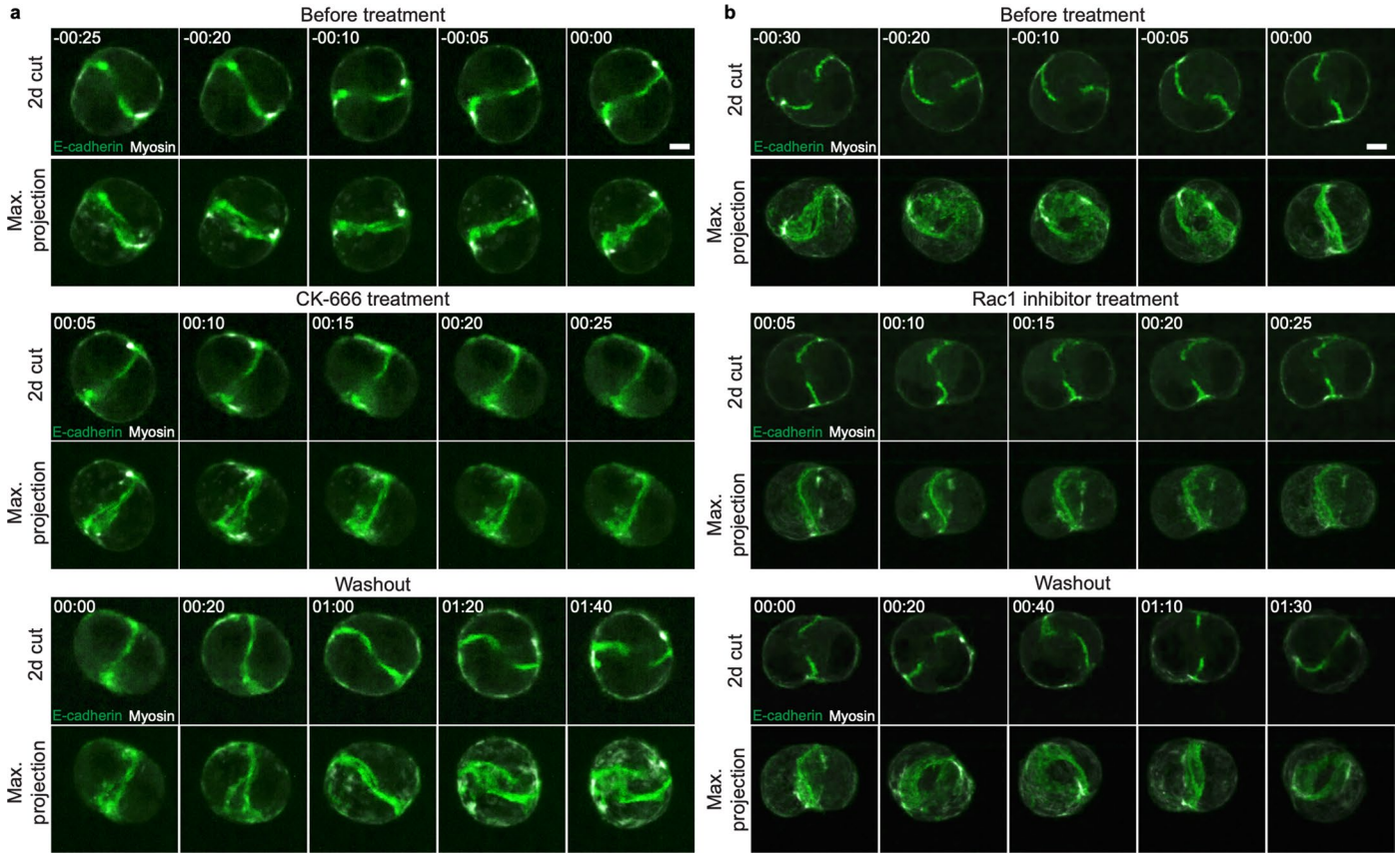

Extended Data Fig. 10 | Interfering with actin dynamics affects doublet rotation. a. Snapshots of a rotating doublet in the presence of the Arp2/3 inhibitor CK-666 before and after incubation followed by washout (see Supplementary Video 13). E-cadherin (green), myosin (grey). Representative example of n > 10 doublets. **b**. Snapshots of a rotating doublet in the presence of Rac1 inhibitor before and after incubation followed by washout (see Supplementary Video 14). E-cadherin (green). Myosin (grey). Representative example of n > 10 doublets. Scale bars: 5 μm. Time in hh:mm.

nature portfolio

Corresponding author(s): Daniel Riveline, Guillaume Salbreux
riveline@unistra.fr,
guillaume.salbreux@unige.ch

Last updated by author(s): 29/01/2024

Reporting Summary

Nature Portfolio wishes to improve the reproducibility of the work that we publish. This form provides structure for consistency and transparency in reporting. For further information on Nature Portfolio policies, see our Editorial Policies and the Editorial Policy Checklist.

Statistics

For all statistical analyses, confirm that the following items are present in the figure legend, table legend, main text, or Methods section.

n/a	Confirmed	
☐	☒	The exact sample size (*n*) for each experimental group/condition, given as a discrete number and unit of measurement
☐	☒	A statement on whether measurements were taken from distinct samples or whether the same sample was measured repeatedly
☐	☒	The statistical test(s) used AND whether they are one- or two-sided *Only common tests should be described solely by name; describe more complex techniques in the Methods section.*
☐	☒	A description of all covariates tested
☐	☒	A description of any assumptions or corrections, such as tests of normality and adjustment for multiple comparisons
☐	☒	A full description of the statistical parameters including central tendency (e.g. means) or other basic estimates (e.g. regression coefficient) AND variation (e.g. standard deviation) or associated estimates of uncertainty (e.g. confidence intervals)
☐	☒	For null hypothesis testing, the test statistic (e.g. *F*, *t*, *r*) with confidence intervals, effect sizes, degrees of freedom and *P* value noted *Give P values as exact values whenever suitable.*
☒	☐	For Bayesian analysis, information on the choice of priors and Markov chain Monte Carlo settings
☒	☐	For hierarchical and complex designs, identification of the appropriate level for tests and full reporting of outcomes
☐	☒	Estimates of effect sizes (e.g. Cohen's *d*, Pearson's *r*), indicating how they were calculated

Our web collection on statistics for biologists contains articles on many of the points above.

Software and code

Policy information about availability of computer code

Data collection	Metamorph was used to acquire the images on a Leica Spinning Disk microscope as described in the Methods section. Simulation results were generated using a custom C++ code adapted from a previously published code available at https://github.com/torressancheza/ias .
Data analysis	FIJI was used to contrast and overlay images. Cell segmentation was performed with previously published FIJI plugin LimeSeg 0.4.2 (https://imagej.net/plugins/limeseg). All quantifications and data analysis were then performed using custom Python codes as described in the Methods section and Supplementary Information. Visualisation and rendering of 3D meshes were performed using Paraview Software 5.10.1. All plots were generated with Python (version 3.9.10).

For manuscripts utilizing custom algorithms or software that are central to the research but not yet described in published literature, software must be made available to editors and reviewers. We strongly encourage code deposition in a community repository (e.g. GitHub). See the Nature Portfolio guidelines for submitting code & software for further information.

Data

Policy information about availability of data

All manuscripts must include a data availability statement. This statement should provide the following information, where applicable:

- Accession codes, unique identifiers, or web links for publicly available datasets
- A description of any restrictions on data availability
- For clinical datasets or third party data, please ensure that the statement adheres to our policy

All data are available upon request to the corresponding authors.

Human research participants

Policy information about studies involving human research participants and Sex and Gender in Research.

Reporting on sex and gender	n/a
Population characteristics	n/a
Recruitment	n/a
Ethics oversight	n/a

Note that full information on the approval of the study protocol must also be provided in the manuscript.

Field-specific reporting

Please select the one below that is the best fit for your research. If you are not sure, read the appropriate sections before making your selection.

☒ Life sciences ☐ Behavioural & social sciences ☐ Ecological, evolutionary & environmental sciences

For a reference copy of the document with all sections, see nature.com/documents/nr-reporting-summary-flat.pdf

Life sciences study design

All studies must disclose on these points even when the disclosure is negative.

Sample size	All quantifications were performed for at least n=12 cell doublets, except for Fig. 5b,c (4 doublets), Fig.5e (9 doublets), Fig. 5g,h (9 doublets) and Ext. Fig. 1c (red curve, 6 doublets).
Data exclusions	No points were excluded from the data analysis.
Replication	All experiments were systematically performed at least 3 times and gave similar results.
Randomization	Cell doublets were chosen to be imaged randomly among a large population. The subset of doublets used for segmentation were chosen randomly among those with a rotation axis approximatively aligned with the microscope Z-axis (with random clockwise or counterwise rotation). This allowed better segmentation of cells.
Blinding	n/a

Reporting for specific materials, systems and methods

We require information from authors about some types of materials, experimental systems and methods used in many studies. Here, indicate whether each material, system or method listed is relevant to your study. If you are not sure if a list item applies to your research, read the appropriate section before selecting a response.

Materials & experimental systems

n/a	Involved in the study
☐	☒ Antibodies
☐	☒ Eukaryotic cell lines
☒	☐ Palaeontology and archaeology
☒	☐ Animals and other organisms
☒	☐ Clinical data
☒	☐ Dual use research of concern

Methods

n/a	Involved in the study
☒	☐ ChIP-seq
☒	☐ Flow cytometry
☒	☐ MRI-based neuroimaging

Antibodies

Antibodies used

1. Rat monoclonal Anti-E-cadherin, Abcam, Cat# Ab11512.
2. Rabbit Polyclonal Anti-Phospho-Myosin Light Chain2 (Cell signaling technology, #3674).
3. Rabbit monoclonal Anti-Paxillin (Abcam, Ab32084).
4. Alexa FluorTM 357 Phalloidin 488 (Thermo Fisher, A12379).

Validation

Validated by the Companies.

Eukaryotic cell lines

Policy information about cell lines and Sex and Gender in Research

Cell line source(s)

1. MDCK II VASP-GFP (see ref. 34).
2. MDCK II MRLC-KO1/E-cadherin-mNG and MDCK II MRLC-GFP (Riveline Lab.).
3. MDCK II E-cadherin-GFP and MDCK II E-cadherin-DsRed (from Nelson, see ref. 37).
4. MDCK II E-cadherin-GFP/Podocalyxin-mScarlett/Halo-CAAX (engineered in Honigmann Lab)
5. MDCK II iLID-LARG::mVenus - 2xrGBD-dTomato - MRLC-iRFP703 (optogenetic cell line, Riveline Lab.).
6. MDCK II Actin-GFP (Nelson Lab)
7. MDCK II Lifeact-iRFP (Riveline Lab)
8. MDCK II E-cadherin-KO (from Ladoux lab, ref. 16)

Authentication

From the sources.

Mycoplasma contamination

All cell lines were checked for the absence of mycoplasma contamination.

Commonly misidentified lines
(See ICLAC register)

No commonly misidentified cell lines were used in the study.